SUBMITTED TO APJ ON 2015 NOVEMBER 23

Preprint typeset using LaTeX style emulateapj v. 01/23/15

arXiv:1511.07443v1 [astro-ph.HE] 23 Nov 2015

TWO DIMENSIONAL CORE-COLLAPSE SUPERNOVA EXPLOSIONS AIDED BY GENERAL RELATIVITY WITH MULTIDIMENSIONAL NEUTRINO TRANSPORT

EVAN O'CONNOR[1,6] AND SEAN M. COUCH[2,3,4,5]

[1]North Carolina State University, Department of Physics, Campus Code 8202, Raleigh, North Carolina, 27695, USA, evanoconnor@ncsu.edu

[2]Department of Physics and Astronomy, Michigan State University, East Lansing, MI 48824, USA; couch@pa.msu.edu

[3]Department of Computational Mathematics, Science, and Engineering, Michigan State University, East Lansing, MI 48824, USA

[4]National Superconducting Cyclotron Laboratory, Michigan State University, East Lansing, MI 48824, USA

[5]Joint Institute for Nuclear Astrophysics, Michigan State University, East Lansing, MI 48824, USA

Submitted to ApJ on 2015 November 23

ABSTRACT

We present results from computational simulations of core-collapse supernovae in FLASH using a newly-implemented multidimensional neutrino transport scheme and a newly-implemented general relativistic (GR) treatment of gravity. For the neutrino transport, we use a two moment method with an analytic closure (so-called M1 transport). This transport is multienergy, multispecies and truly multidimensional since we do not assume the commonly used ray-by-ray approximation. Our GR gravity is implemented in our Newtonian hydrodynamics simulations via an effective relativistic potential that closely reproduces the GR structure of neutron stars and has been shown to match GR simulations of core collapse quite well. In axisymmetry, we simulate core-collapse supernovae with five different progenitor models in both Newtonian and GR gravity. We find that the more compact protoneutron star structure realized in simulations with GR gravity gives higher neutrino luminosities and higher neutrino energies. These differences in turn give higher neutrino heating rates ($\sim$20-30% over the corresponding Newtonian gravity simulations) which increases the efficacy of the neutrino mechanism. All five models fail to explode in Newtonian gravity while three of the five models successfully explode, albeit weakly, in GR gravity. Our results, both in Newtonian and GR gravity, compare well with several other studies in the literature. These results conclusively show that the approximation of Newtonian gravity for simulating the core-collapse supernova central engine is not acceptable.

Keywords: hydrodynamics - neutrinos - radiative transfer - stars: neutron - stars: supernovae: general - methods: numerical

1. INTRODUCTION

Core-collapse supernovae mark the end stage of stellar evolution for massive stars. These explosions are initiated in the cores of stars with zero-age main sequence masses above 8-10 $M_\odot$, where hydrostatic burning of progressively heavier and heavier elements culminates in the formation of a degenerate and inert iron core with a mass of at least $\sim$1.2 $M_\odot$. The stability of this iron core against gravitational collapse is due to electron degeneracy pressure. However, once the iron core grows beyond the effective Chandrasekhar mass, which can vary depending on the central entropy and electron fraction (Baron & Cooperstein 1990), the core begins to collapse. The collapse is halted when the matter reaches nuclear density at which point the repulsive core of the strong nuclear force can supply enough pressure to stabilize the material once again. The inertia of the collapsing inner core causes it to overshoot the new hydrostatic equilibrium, the rebounding of the core is responsible for launching a shock wave into the still-collapsing outer mantle of the iron core. For a successful core-collapse supernova, this shock will ultimately unbind most of the mass of star and help spread the nucleosynthetic products of stellar evolution throughout the host galaxy. However, the shock expansion is hampered by two main sinks of energy. First, the dissociation of the heavy nuclei into neutron and protons as they pass through the shock gives an inefficient conversion of the kinetic energy of the infalling material into thermal energy behind the shock as a modest fraction must go into the internal energy of the matter. Second, the temperature behind the shock, and the abundance of free protons now available for electron capture, facilitate energy loss via neutrino emission. This also removes thermal energy from behind the shock. Both of these processes reduce the thermal pressure behind the shock and bring it into equilibrium with the ram pressure of the infalling matter. This causes the shock to stall and become an accretion shock. The goal of core-collapse supernova theory over the last $\sim$50 years has been to understand the shock revival mechanism. The most ubiquitous mechanism has been the neutrino heating mechanism (Colgate & White 1966; Bethe & Wilson 1985). Neutrino heating is always found in core collapse simulations. The intense neutrino radiation field streaming away from the protoneutron star (PNS) quickly falls out of equilibrium with the matter near the neutrinosphere. Outside this radius there are lingering charged-current interactions of electron type neutrinos and antineutrinos on matter where a net positive transfer of energy between the neutrinos and the matter occurs. If this energy transfer is sufficient, it can lead to shock expansion and a successful explosion. In spherically symmetric simulations of the collapse of typical iron cores, the amount of neutrino heating is not sufficient to drive an explosion (Liebendörfer et al. 2001; Rampp & Janka 2002). Explosions in two and three dimensional models with energy-dependent neutrino transport have been reported over the last

[6] Hubble Fellow

~5 years (Marek & Janka 2009; Suwa et al. 2010; Müller et al. 2012b,a; Takiwaki et al. 2012; Bruenn et al. 2013, 2014; Nakamura et al. 2015; Suwa et al. 2014; Lentz et al. 2015; Pan et al. 2015), however in this set of successful explosions there are large discrepancies amongst the results from different codes for otherwise very similar initial conditions and input physics.

Many of the earliest simulations of core-collapse supernova used or were concerned with a general relativistic (GR) approach (Colgate & White 1966; May & White 1966; Misner & Sharp 1964; Wilson 1971; Bruenn 1985; Burrows 1988), and rightly so since neutron stars are sufficiently compact that GR dramatically effects their equilibrium structure. While the importance of including GR gravity in simulations core-collapse supernovae has always persisted in the literature and is in use in many current and state-of-the-art multidimensional, core-collapse supernova calculations (Bruenn et al. 2013, 2014; Müller et al. 2012b; Marek & Janka 2009; Ott et al. 2013; Kuroda et al. 2012; Lentz et al. 2015), many modern simulations use a purely Newtonian approximation for gravity (Takiwaki et al. 2014; Nakamura et al. 2015; Suwa et al. 2014; Couch & O'Connor 2014; Handy et al. 2014; Dolence et al. 2015; Couch & Ott 2015; Pan et al. 2015). Liebendörfer et al. (2001) extensively compared GR gravity and Newtonian gravity in spherical symmetry with a full Boltzmann neutrino transport solver. While their baseline simulations in both prescriptions of gravity fail to explode in 1D, their conclusion is that, overall, GR is helpful for the development of the core-collapse supernova explosion. This conclusion comes out of serendipitous simulations where incorrect nucleon isoenergetic scattering cross sections were used. In these simulations, when GR gravity was used, the simulation predicted an explosion, but when Newtonian gravity was used, the simulations failed to achieve explosions. Buras et al. (2006) and Lentz et al. (2012) also compared Newtonian and GR simulations in spherical symmetry with energy dependent neutrino transport. Like Liebendörfer et al. (2001), they observe higher neutrino luminosities and energies but do not extensively study the differences, in part because both simulations still fail to explode owing to the 1D nature of the simulations. Kuroda et al. (2012) examined the difference between special relativistic hydrodynamics and GR hydrodynamics in both 1D and 3D core-collapse simulations using approximate neutrino transport (a grey M1 scheme). However, while the 3D GR simulations show signs of increased susceptibility to explosion, the simulated time was not long enough to observe an explosion. Müller et al. (2012b) also investigated the influence of Newtonian gravity, GR gravity, and GR effective potential gravity in 2D core collapse simulations using a variable Eddington factor, two-moment, energy dependent neutrino transport scheme and the ray-by-ray+ approximation (where the neutrino transport is done along radial rays assuming spherical symmetry and with minimal coupling between neighboring rays). For the classic $15\,M_\odot$ model from Woosley & Weaver (1995), Müller et al. (2012b) find a late and asymmetric explosion when using fully GR gravity, but not with Newtonian gravity, GR effective potential gravity, or with reduced set neutrino opacities. This was, and still is, the most direct evidence that GR aids in the explosion mechanism. It is important to validate the hypothesis that GR gravity does indeed lead to more favorable conditions for explosion in modern day simulations, with updated progenitor models, and loosening the spherically symmetric assumption.

A number of two-dimensional simulations with similar initial conditions have been performed by several different groups using various different treatments of energy-dependent neutrino transport. The initial conditions, chosen by Bruenn et al. (2013), consists of four models from Woosley & Heger (2007) with zero-age main sequence masses of $12\,M_\odot$, $15\,M_\odot$, $20\,M_\odot$, and $25\,M_\odot$. They employ the EOS of Lattimer & Swesty (1991) with incompressibility parameter $K_0 = 220$ MeV (hereafter, LS220). Simulations of these four models, and the same EOS were also presented by Hanke (2014). Both Bruenn et al. (2013) and Hanke (2014) use Newtonian hydrodynamics with a GR effective potential (Marek et al. 2006, Case A). Dolence et al. (2015) also simulate core collapse in these progenitors, however they use the Shen et al. (2011) EOS and assume purely Newtonian gravity. Suwa et al. (2014) simulate three of the four models, use the LS220 EOS, and Newtonian gravity. More details about these simulations can be found in Table 1 and the various references. While no collaborative comparison has been done for these simulations, they do represent the largest set of recent multidimensional core-collapse supernova models performed by multiple simulation codes. In Table 1, we include the outcome of these simulations (explosion/no explosion) as well as the time of explosion for successful models, we divide the results into simulations with a GR treatment of gravity, and with a Newtonian treatment of gravity. The results are quite disparate. Bruenn et al. (2013) find early and energetic explosions in all four simulated models while Hanke (2014) finds explosions in all models, but some explosions are quite delayed (up to ~500 ms later than Bruenn et al. 2013). Furthermore, Hanke (2014) conclude that the final explosion energies will be significantly lower than Bruenn et al. (2013). For the simulations with Newtonian gravity, Dolence et al. (2015) find no explosions and Suwa et al. (2014) finds an explosion in one model, the $12\,M_\odot$ progenitor.

In this paper, we perform core collapse simulations for this same set of progenitors and employ the LS220 EOS (Lattimer & Swesty 1991; O'Connor & Ott 2010). We use a new multidimensional neutrino transport implementation in the `FLASH` hydrodynamics simulation package (Fryxell et al. 2000; Dubey et al. 2009). We also systematically explore the differences between core collapse simulations with Newtonian gravity and with a newly implemented GR effective potential. We include our results in Table 1. Our main conclusion is that a GR treatment of gravity is important and required for accurately simulating the neutrino mechanism in core-collapse supernovae. The assumption of Newtonian gravity underestimates the neutrino luminosity and the mean energies of the emitted spectra, consequently, Newtonian gravity results in lower neutrino heating rates in the gain region. Given the large number of simulation groups currently using Newtonian gravity to study core-collapse supernovae, we find it especially important to systematically demonstrate this point. We also compare our results to other core-collapse supernova simulations with comparable initial conditions. In some cases we find close agreement with these other studies, particularly with the results of the Hanke (2014).

The remainder of this paper is organized as follows. In §2, we introduce the methods used for computing the GR effective potential and for our neutrino transport scheme. Several tests of these methods are presented in the Appendix. In §3 we present our main results including a detailed comparison to publicly available simulation data from Liebendörfer et al.

(2005) and O'Connor (2015), multidimensional results assuming Newtonian gravity, and multidimensional results using GR effective potential gravity. We discuss our Newtonian vs. GR results in §4 as well as compare our results with those available in the literature for the same progenitor models and gravity prescriptions. We conclude in §5.

2. METHODS

2.1. *Effective General Relativistic Potential*

For our implementation of GR gravity we do not directly solve Einstein's equations, rather we take an approximate and much simpler approach. We perform our hydrodynamic simulations using standard Newtonian hydrodynamics. However, for the gravity potential, we replace the standard monopole contribution to the Newtonian gravitational potential with an effective GR potential empirically derived from modified GR structure equations. The formulation we use was presented in Keil (1997); Rampp & Janka (2002) and later improved by Marek et al. (2006). In spherical symmetry, the Newtonian gravitational potential can be determined via the differential equation,

$$\frac{d\phi_{\rm NW}}{dr} = \frac{Gm(r)}{r^2}\,, \tag{1}$$

where $m(r)$ is the enclosed mass determined via,

$$\frac{dm}{dr} = 4\pi r^2 \rho\,, \tag{2}$$

where ρ is the mass density. For Newtonian gravity, the boundary condition on the enclosed mass is $m(r=0)=0$, while the condition on the potential is that at the surface of the star,

$$\phi_{\rm NW,surface} = -GM_{\rm star}/r_{\rm surface}\,. \tag{3}$$

Marek et al. (2006) modify these equations, using instead,

$$\frac{d\phi_{\rm eff}}{dr} = G\frac{m_{\rm TOV}(r)+4\pi r^3(P+P_\nu)/c^2}{r^2\Gamma^2}\left[\frac{\rho+\rho\epsilon/c^2+P/c^2}{\rho}\right], \tag{4}$$

where P, P_ν, and ϵ are the matter pressure, neutrino pressure, and specific internal energy, respectively. We take the same boundary condition as Newtonian gravity, $\phi_{\rm eff,surface} = -GM_{\rm star}/r_{\rm surface}$. Γ is taken to be,

$$\Gamma = \left[1+v^2/c^2-\frac{2Gm_{\rm TOV}(r)}{rc^2}\right]^{1/2}, \tag{5}$$

and $m_{\rm TOV}(r)$ is still the enclosed mass, but rather than Eq. 2, Marek et al. (2006) ultimately suggests to take the enclosed mass as the solution to the following differential equation,

$$\frac{dm_{\rm TOV}}{dr} = 4\pi r^2(\rho+\rho\epsilon/c^2+E_\nu+\frac{v_i F^i_\nu}{\Gamma})\times\Gamma\,. \tag{6}$$

$m_{\rm TOV}$, similar to the Tolman-Oppenheimer-Volkoff (TOV) mass, accounts for internal matter energy, and in this case, the energy and momentum of the neutrinos (E_ν and F^i_ν, respectively). Since we ignore velocity dependence in our transport equations, we drop the $v_i F^i_\nu$ term in this work. The factor of Γ, which is not a part of the standard TOV mass, was empirically found by Marek et al. (2006) to better reproduce actual GR calculations. This is the 'case A' GR effective potential of Marek et al. (2006). In the Appendix we perform an unstable neutron star migration test, in both 1D and 2D, and obtain results consistent with Marek et al. (2006). We have also tested black hole formation in our FLASH implementation using the $40M_\odot$ progenitor model from Woosley & Heger (2007). We find a black hole formation time that is ∼556 ms, or ∼21 ms later than the full GR simulations from O'Connor (2015). Both of these tests give us confidence that our implementation of the GR effective potential is consistent with that of Marek et al. (2006) and close to true GR gravity.

For practical implementation in FLASH, since we use a cylindrical grid, we must spherically average the matter and neutrino fields to obtain ρ, P, P_ν, ϵ, v, and E_ν as a function of radius. We take the grid center as the center of our spherical average. We then numerically solve Eq. 6 and Eq. 5 iteratively as Γ depends on $m_{\rm TOV}$ and vice versa. After solving for these terms, we integrate Eq. 4 to obtain the spherically symmetric gravitational potential. For the 2D simulations (both Newtonian gravity and effective GR gravity) presented here we only use the monopole term for determining the total gravitational potential.

2.2. *Neutrino Radiation Transport*

We implement a truly multidimensional, two-moment, energy-dependent, multispecies, neutrino radiation transport scheme with an analytic closure in FLASH. Our implementation follows closely that of O'Connor & Ott (2013) which is based on the formalisms of Shibata et al. (2011). In order to incorporate general relativistic aspects into the transport we follow the assumptions of Rampp & Janka (2002), however, for this work, we ignore the distinction between the fluid rest frame and the coordinate frame as well as any coupling between neutrino energy groups, either from gradients in the fluid velocity or the gravitational potential, as well as inelastic neutrino scattering processes. With these assumptions, the evolution equations for the zeroth (E; neutrino energy density) and first (F^i; neutrino momentum density) energy-dependent neutrino moments are, in spherical symmetry,

$$\partial_t E + \frac{1}{r^2}\partial_r[\alpha r^2 F^r] = \alpha[\eta-\kappa_a E] - \alpha F^r\partial_r\phi\,, \tag{7}$$

$$\partial_t F^r + \frac{1}{r^2}\partial_r[\alpha r^2 P^{rr}] = -\alpha[\kappa_s+\kappa_a]F^r + \alpha\frac{P^{\theta\theta}+P^{\phi\phi}}{r} - \alpha E\partial_r\phi\,, \tag{8}$$

and cylindrical symmetry,

$$\partial_t E + \frac{1}{r}\partial_r[\alpha r F^r] + \partial_z[\alpha F^z] = \alpha[\eta-\kappa_a E] - \alpha F^i\partial_i\phi\,, \tag{9}$$

$$\partial_t F^r + \frac{1}{r}\partial_r[\alpha r P^{rr}] + \partial_z[\alpha P^{zr}] = -\alpha[\kappa_s+\kappa_a]F^r + \alpha\frac{P^{\phi\phi}}{r} - \alpha E\partial_r\phi\,, \tag{10}$$

$$\partial_t F^z + \frac{1}{r}\partial_r[\alpha r P^{rz}] + \partial_z[\alpha P^{zz}] = -\alpha[\kappa_s+\kappa_a]F^z - \alpha E\partial_z\phi\,. \tag{11}$$

In these equations, P^{ij} is the second moment of the neutrino distribution function, which we approximate via a closure relation described below. $\alpha = \exp(\phi/c^2)$ is the lapse and ϕ is the gravitational potential from Eq. 4. In our Newtonian simulations these general relativistic terms do not appear in the

Table 1

Reference	Gravity	EOS	Grid	ν Treatment	s12		s15		s20		s25	
					Exp?	$t_{\rm exp}$ [s]	Exp?	$t_{\rm exp}$ [s]	Exp?	$t_{\rm exp}$ [s]	Exp?	$t_{\rm exp}$ [s]
Bruenn et al. (2013)	GREP	LS220	Spherical	MGFLD RxR+	Yes	0.236	Yes	0.233	Yes	0.208	Yes	0.212
Hanke (2014)	GREP	LS220	Spherical	VEF RxR+	Yes	0.79	Yes	0.62	Yes	0.32	Yes	0.40
this work	GREP	LS220	Cylindrical	MG M1	No	–	Yes	0.737	Yes	0.396	Yes	0.350
Dolence et al. (2015)	NW	H. Shen	Cylindrical	MGFLD	No	–	No	–	No	–	No	–
Suwa et al. (2014)	NW	LS220	Spherical	IDSA RxR	Yes	0.425	No	–	No	–	N/A	N/A
this work	NW	LS220	Cylindrical	MG M1	No	–	No	–	No	–	No	–

Note. — GREP gravity is used to denote Newtonian hydrodynamic simulations with an effective, spherically symmetric, GR potential instead of the Newtonian monopole term. NW gravity is pure Newtonian gravity. The LS220 EOS is the Lattimer & Swesty (1991) $K_0 = 220$ MeV EOS while H. Shen is the EOS from Shen et al. (2011). The neutrino treatment in Bruenn et al. (2013) is multigroup flux-limited diffusion (MGFLD) and in Hanke (2014) is a two moment scheme with the closure solved by a model Boltzmann equation. Both of these transport schemes use the the ray-by-ray+ (RxR+) approximation for the multidimensional transport treatment where the transport is solved only in the radial direction (along rays). The '+' refers to the addition of advection of neutrinos in the lateral direction in optically thick regions. Dolence et al. (2015) use MGFLD as well, but solve the multidimensional transport directly. Suwa et al. (2014) employ the isotropic diffusion source approximation, akin to MGFLD, and use the ray-by-ray approximation. Bruenn et al. (2013) defines the explosion time as the postbounce time when the shock reaches 500 km. We use this definition for extracting the explosion time from Suwa et al. (2014). Hanke (2014) only shows shock radius data to 400 km, therefore we use the postbounce time when the shock reaches this radius. However, this makes no qualitative difference since the shock expansion is quite rapid at this time. We also show the results of this work. We use the abbreviation MG M1 to denote multigroup M1 neutrino transport.

moment evolution equations (i.e. $\alpha = 1; \partial_i \phi = 0$). Finally, η, κ_a, and κ_s are the neutrino emissivity, absorption opacity, and scattering opacity, respectively, which depend on the local density, temperature, and electron fraction as well as the neutrino species and energy. For the remainder of this section we describe the numerical techniques used to solve these equations and the microphysics used to compute the neutrino interaction coefficients.

Closure: To close the hierarchy of moment evolution equations after the first two moments, we must specify a closure relation for the Eddington tensor P^{ij} in terms of the two lower moments E and F^i. We choose the common M1 closure. In regions where the radiation is isotropic, $P^{ij} \equiv P^{ij}_{\rm thick} = \delta^{ij} E/3$ and in regions far from the source, $P^{ij} \equiv P^{ij}_{\rm thin} = E(F^i F^j/F^2)$. Therefore, for our Eddington tensor, we choose a common interpolation between these two limiting regimes,

$$P^{ij} = \frac{3(1-\chi)}{2} P^{ij}_{\rm thick} + \frac{3\chi - 1}{2} P^{ij}_{\rm thin}\,, \tag{12}$$

or, using the expressions mentioned above,

$$P^{ij} = \left[\frac{3(1-\chi)}{2} \frac{\delta^{ij}}{3} + \frac{3\chi-1}{2} \frac{F^i F^j}{F^2} \right] E\,. \tag{13}$$

In these equations χ is taken to be

$$\chi = \frac{1}{3} + \frac{2}{15}(3f^2 - f^3 + 3f^4)\,, \tag{14}$$

where $f \equiv (F^i F_i/E^2)^{1/2}$ is the flux factor. f is equal to 0 if the radiation is isotropic, which gives a $\chi = 1/3$ and $P^{ij} = P^{ij}_{\rm thick}$. f is 1 if the radiation is fully forward peaked in some direction. For this case, $\chi = 1$ and $P^{ij} = P^{ij}_{\rm thin}$.

Explicit Fluxes: For computing the spatial flux terms on the left hand side of Eq. 7-Eq. 11, we use finite differencing,

$$\partial_x [\alpha r^m F^x] = \frac{(\alpha r^m)_{(k+1/2)} \mathcal{F}_{(k+1/2)} - (\alpha r^m)_{(k-1/2)} \mathcal{F}_{(k-1/2)}}{\Delta x}\,, \tag{15}$$

and

$$\partial_x [\alpha r^m P^{xi}] = \frac{(\alpha r^m)_{(k+1/2)} \mathcal{P}^i_{(k+1/2)} - (\alpha r^m)_{(k-1/2)} \mathcal{P}^i_{(k-1/2)}}{\Delta x}\,, \tag{16}$$

where m is either $0, 1, 2$. To obtain the interface fluxes $\mathcal{F}_{(k+1/2)}$ and $\mathcal{P}^i_{(k+1/2)}$, we use the standard HLLE Riemann solver for hyperbolic equations. For the flux evaluation at an interface $(k+1/2)$, we reconstruct E and F^i/E to both sides of the zone interfaces using 2nd-order TVD (total variation diminishing) interpolation. On both sides of the interface we recompute the closure via Eq. (13) to obtain the cell interface values of P_{ij}. The characteristic speeds for the Riemann solver are calculated in a similar way as the closure in that we interpolate between the optically thick and optically thin limits. First, for each interface (characterized here by the direction k), we determine the minimum and maximum speeds on each side of the interface in both the optically thin and optically thick limits. For the optically thick limit the choice is clear,

$$\lambda^{(k)}_{\rm thick,min} = -\frac{1}{\sqrt{3}}; \lambda^{(k)}_{\rm thick,max} = +\frac{1}{\sqrt{3}}\,. \tag{17}$$

For the thin limit, and our choice of closure, the maximum and minimum characteristic speeds are (Shibata et al. 2011)

$$\lambda^{(k)}_{\rm thin,min/max} = \min/\max\left(\frac{\pm F^k}{\sqrt{F_i F^i}}, E\frac{F^k}{F_i F^i} \right). \tag{18}$$

Next, to determine the maximum and minimum speed on each side of the interface we interpolate between the optically thick ($\lambda^{(k)}_{\rm thick}$) and free streaming ($\lambda^{(k)}_{\rm thin}$) regimes via,

$$\lambda^{(k)}_{\rm min/max} = \frac{3(1-\chi)}{2} \lambda^{(k)}_{\rm thick,min/max} + \frac{3\chi-1}{2} \lambda^{(k)}_{\rm thin,min/max}\,. \tag{19}$$

The final step to determine the minimum and maximum speeds for the Riemann solver is to take $\lambda^{(k),+} = \max(\lambda^{(k),(R)}_{\rm max}, \lambda^{(k),(L)}_{\rm max})$ and $\lambda^{(k),-} = \min(\lambda^{(k),(R)}_{\rm min}, \lambda^{(k),(L)}_{\rm min})$. Where (R) and (L) denote the right and left side of the interface, respectively.

With the reconstructed moments and minimum and maximum characteristic speeds in hand, the HLLE Riemann solution for the fluxes at the interface is then,

$$\mathcal{F}_{(k+1/2),\rm HLLE} = \frac{\lambda^{(k),+} F^{k,(L)} - \lambda^{(k),-} F^{k,(R)} + \lambda^{(k),+}\lambda^{(k),-}(E^{(R)} - E^{(L)})}{\lambda^{(k),+} - \lambda^{(k),-}} \tag{20}$$

and

$$\mathcal{P}^j_{(k+1/2),\rm HLLE} = \frac{\lambda^{(k),+} P^{(L)}_{kj} - \lambda^{(k),-} P^{(R)}_{kj} + \lambda^{(k),+}\lambda^{(k),-}(F^{(R)}_j - F^{(L)}_j)}{\lambda^{(k),+} - \lambda^{(k),-}} \tag{21}$$

where here (R) and (L) label the reconstructed (or recalculated for P^{ij}) moments on the right and left side of the interface $k+1/2$, respectively.

However, this solution relies on the equations being hyperbolic. This condition is violated in regions with high opacity and numerical diffusion can dominant the HLLE Riemann solution. The transition away from hyperbolicity can be traced via the Peclet number ($\mathrm{Pe} \equiv \Delta x(\kappa_s + \kappa_a)$). If Pe is $\gtrsim 1$ then we must correct the Riemann solution. We follow Audit et al. (2002); O'Connor & Ott (2013) and ultimately take the following for the interface fluxes,

$$\mathcal{F}_{(k+1/2)} = \frac{\lambda^{(k),+}F^{k,(L)} - \lambda^{(k),-}F^{k,(R)} + \epsilon\lambda^{(k),+}\lambda^{(k),-}(E^{(R)} - E^{(L)})}{\lambda^{(k),+} - \lambda^{(k),-}} \tag{22}$$

and

$$\mathcal{P}^{j}_{(k+1/2)} = \frac{\epsilon^2(\lambda^{(k),+}P^{(L)}_{kj} - \lambda^{(k),-}P^{(R)}_{kj}) + \epsilon\lambda^{(k),+}\lambda^{(k),-}(F^{(R)}_{j} - F^{(L)}_{j})}{\lambda^{(k),+} - \lambda^{(k),-}} + (1-\epsilon^2)\frac{P^{(R)}_{kj} + P^{(L)}_{kj}}{2} \tag{23}$$

where $\epsilon = \min(1, 1/\mathrm{Pe})$.

In the Appendix, we perform a 2D shadow test to ensure the correct multidimensional implementation of our transport scheme. There we show one of the beneficial features of M1, the ability to maintain neutrino momentum in the free streaming regime. In one moment transport schemes, like flux limited diffusion, the flux of neutrinos is determined by the spatial gradient of the zeroth moment. In the context of core-collapse supernovae, this can cause a smoothing out of the radiation field at large distances (Ott et al. 2008).

Neutrino Interactions: The last aspect of the neutrino moment evolution equations (Eq. 7-Eq. 11) are the neutrino interaction coefficients. These coefficients are interpolated from a table computed via `NuLib` (O'Connor 2015), an open-source neutrino interaction library. We include a basic set of neutrino interactions and study three independent neutrino species: electron neutrino ν_e, electron antineutrino $\bar{\nu}_e$, and a characteristic heavy-lepton neutrino $\nu_x = \{\nu_\mu, \bar{\nu}_\mu, \nu_\tau, \bar{\nu}_\tau\}$. For electron neutrino and electron antineutrino emission processes we include electron and positron capture on protons and neutrons, respectively following Bruenn (1985); Burrows et al. (2006) and include weak magnetism and nucleon recoil corrections from Horowitz (2002). We also include electron neutrino emission via electron capture on heavy nuclei via the simple formalism of Bruenn (1985). Neutrino emissivities are computed from the absorption opacities via Kirchhoff's law which equates the emissivity to the rate of absorption of an equilibrium neutrino distribution: $\eta = \kappa_a E_{\mathrm{equil}}$. Heavy-lepton neutrino emission from electron-positron annihilation and nucleon-nucleon Bremsstrahlung is handled via an approximation which computes an effective emissivity and absorption opacity and does not require energy group coupling. This approach works well for the core collapse problem (O'Connor 2015). We include elastic scattering on neutrons and protons, which also includes weak magnetism and recoil corrections, elastic scattering on alpha particles and on heavy nuclei, with the latter including corrections for the heavy-ion form factor, ion-ion correlations, and electron polarization (Burrows et al. 2006).

Hydrodynamic coupling: During each time step we solve the neutrino moment evolution equations operator-split from the hydrodynamics. We first update the hydrodynamical variables from time step (n) to $(n+1)$ using `FLASH`'s unsplit hydrodynamics solver, third-order reconstruction with PPM (Colella & Woodward 1984), and the HLLC Riemann solver. We then use the updated matter variables ($\rho^{(n+1)}$,$T^{(n+1)}$, and $Y_e^{(n+1)}$) to compute the $(n+1)$ neutrino-matter interaction coefficients, $\eta^{(n+1)}$, $\kappa_a^{(n+1)}$, and $\kappa_s^{(n+1)}$. The spatial flux calculation of the neutrino moment evolution equations is computed from the (n) state radiation variables as described above. For the radiation time step, these fluxes are treated as an explicit source term. The remaining terms, which are all local to each grid zone and only couple the neutrino energy density and momentum density of a given group and species, are solved via implicit integration to arrive at $E^{(n+1)}$ and $F^{i,(n+1)}$. Following the update of the neutrino moments, we compute the energy, momentum, and lepton exchange with the matter and update $T^{(n+1)}$ and $Y_e^{(n+1)}$ operator split. We update the matter momenta via source terms during the hydrodynamic update step. The momenta source terms are also coupled into the hydrodynamic Riemann solver. The use of an operator split method over a coupled method between the radiation and the hydrodynamics is justified because of the small time step imposed by the explicit update of the neutrino radiation fields.

2.3. *FLASH simulation setup*

Both the hydrodynamics and the radiation transport share a common time step that is set by the light crossing time of the smallest grid zone and a Courant factor. We use a cylindrical grid with adaptive mesh refinement (AMR) for our simulations. Unless otherwise stated, our domains extend out to 2×10^9 cm in the radial coordinate, and $\pm2\times10^9$ cm along the cylindrical axis. Our maximum AMR block size is 4×10^8 cm and we allow up to 10 total levels of mesh refinement, giving a minimum AMR block size of $\sim$7.81 km. We perform simulations with two resolutions. Our lower (higher) resolution simulations have 16 (24) cells per dimension and per block resulting in a smallest grid zone with a side width of $\sim$488 m ($\sim$325 m). Using a Courant factor of 0.4 results in a time step of $\sim 6.5\times10^{-7}$ s ($\sim 4.3\times10^{-7}$ s). We refine based on a combination of the second spatial derivatives of the density and pressure. At larger radii, we restrict refinement so as to maintain an effective resolution of at least 0.5 degrees (0.34 degrees in our higher resolution simulations). As a result, we have decrements in refinement at $\sim$107 km, $\sim$215 km, $\sim$430 km, and so on.

3. RESULTS

3.1. *s15WW95 - A Detailed Look*

We use the classic 15 $M_\odot$ core-collapse supernova progenitor profile from Woosley & Weaver (1995) as a test case, denoted throughout as s15WW95. To make comparisons with previous publicly available work (Liebendörfer et al. 2005), we use the Lattimer & Swesty EOS with an incompressibility of 180 MeV (LS180; Lattimer & Swesty 1991). Also following Liebendörfer et al. (2005), we do not include weak magnetism and recoil corrections for the neutrino opacities. We present the results in Fig. 1. In all panels, red lines are collapse calculations using Newtonian gravity, black lines are calculations using our standard general relativistic effective

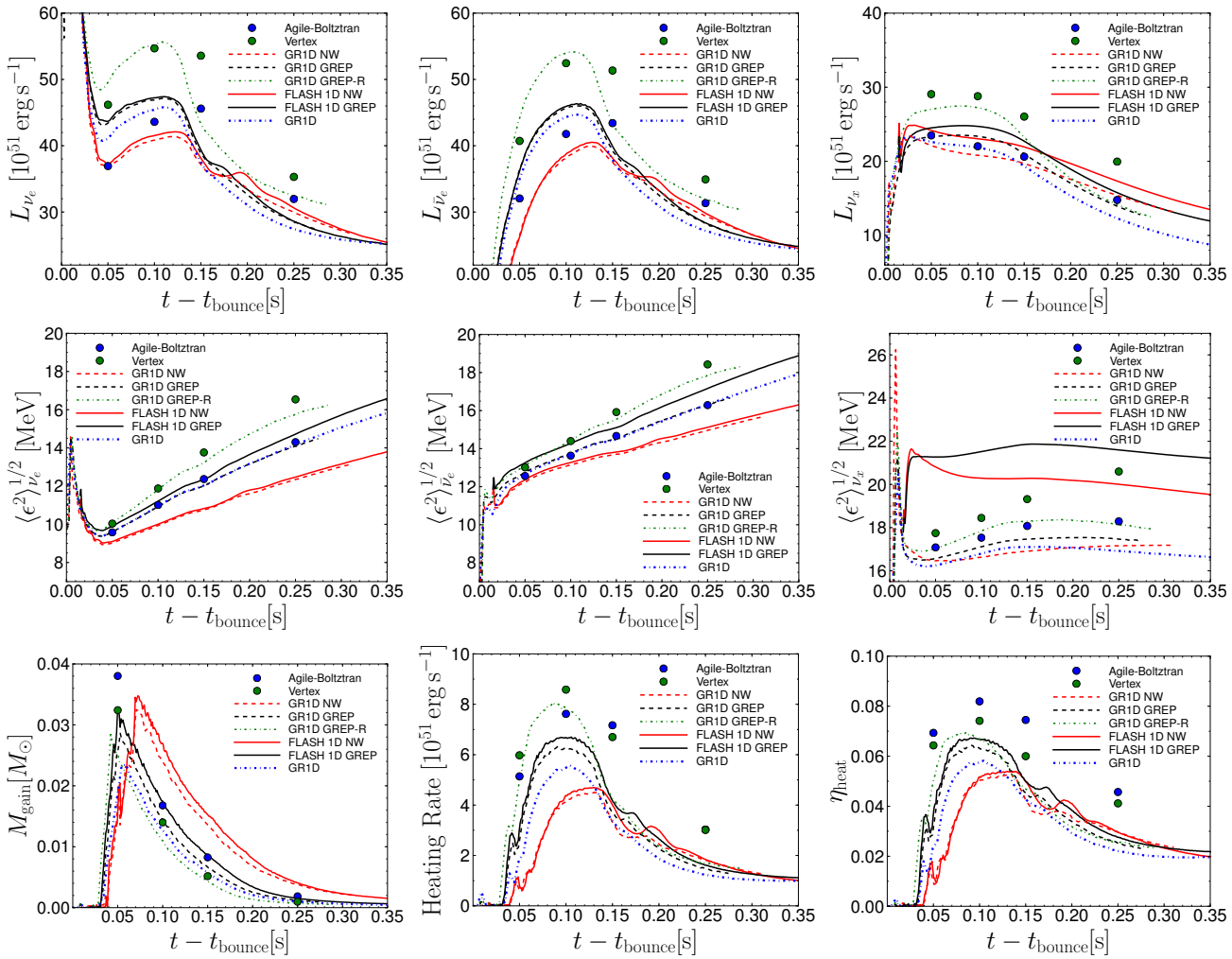

Figure 1. Simulation data from various calculations of the collapse of the s15WW95 progenitor from Woosley & Weaver (1995). Red lines are Newtonian (NW) calculations, black lines are general relativistic calculations using the standard 'case A' effective potential (denoted GREP) from Marek et al. (2006)), the green line uses 'case R' and are to be compared with the `Vertex` data from Liebendörfer et al. (2005) (green dots), finally the blue line is a calculation with `GR1D`'s GR gravity and should be compared to the *Agile*-`Boltztran` data from Liebendörfer et al. (2005) (blue dots). For the red (NW) and black (GREP) lines, dashed lines show data from 1D simulations with `GR1D` while the solid lines show data from spherically symmetric simulations with `FLASH`. All `GR1D` simulations use the full transport of O'Connor (2015), including energy-group coupling, inelastic scattering, and full velocity dependence. All `FLASH` simulations ignore these neutrino processes, and are started from the corresponding `GR1D` run at 15 ms after core bounce. Data from Liebendörfer et al. (2005) is taken at 50, 100, 150, and 250 ms only as at these times the full data from the simulations are given. Note, all luminosities and root mean squared energies are given in the lab frame, and therefore the `Vertex` and *Agile*-`Boltztran` data are converted using $L_\nu^{\rm lab} \sim L_\nu^{\rm fluid}(1+v/c)/(1-v/c)$ and $\sqrt{\langle E^2\rangle_\nu^{\rm lab}} \sim \sqrt{\langle E^2\rangle_\nu^{\rm fluid}}(1+v/c)$.

potential, 'case A', from Marek et al. (2006). The green line (thin dashed-dotted) in Figure 1 uses 'case R' from Marek et al. (2006) and is presented for comparison purposes with the green points, which are data extracted from the publicly available `Vertex` data presented in Liebendörfer et al. (2005). Finally, the blue (thick dashed-dotted) line is from a fully general relativistic calculation using `GR1D` (data is from O'Connor 2015) while blue dots are data taken from publicly available *Agile*-`Boltztran` data from Liebendörfer et al. (2005). For the red and black lines, the thin dashed lines correspond to data taken from `GR1D` and the thick dashed lines are from `FLASH`. We note that all of the `GR1D` simulations (both GREP and full GR) include inelastic scattering of neutrinos on electrons, energy-group coupling, and velocity dependence. These aspects are especially important during the collapse phase, hence, we start all `FLASH` simulations, which ignore these aspects, from `GR1D` profiles at ∼15 ms after bounce. We discuss these approximations in great detail below. Due to the mismatch of fluid-lab frame distribution functions, there are some initial artifacts in the neutrino quantities at that time. For our s15WW95 simulations the outer extent of our domain is taken to be 10^9 cm.

The top and center panels of Fig. 1 show the lab-frame neutrino luminosity and root mean squared energy, respectively, of electron neutrinos (left panels), electron antineutrinos (middle panels), and heavy-lepton neutrinos (right panels) extracted from the simulations at 500 km. For the data from Liebendörfer et al. (2005), we project their fluid frame luminosity to the lab frame via $L_\nu^{\rm lab} \sim L_\nu^{\rm fluid}(1+v/c)/(1-v/c)$ and the root mean squared energy via $\sqrt{\langle\epsilon^2\rangle_\nu^{\rm lab}} \sim \sqrt{\langle\epsilon^2\rangle_\nu^{\rm fluid}}(1+v/c)$. The bottom panels of Fig. 1 show the mass in the gain region (left), the total heating rate in the gain region (middle) and heating efficiency (right). The gain region is defined as the region within the shock, but outside the neutrinosphere, where there is an increasing internal energy of the matter due to neutrino interactions. The heating efficiency is defined as

the ratio of the rate of energy deposition into the gain region ($\dot{Q}^{\rm gain}_{\rm heat}$) to the total electron-type neutrino luminosity at the gain radius. We estimate the latter by adding the heating rate to the lab-frame neutrino luminosity extracted from our simulations,

$$\eta_{\rm heat} = \frac{\dot{Q}^{\rm gain}_{\rm heat}}{L^{\rm lab}_{\nu_e} + L^{\rm lab}_{\bar{\nu}_e} + \dot{Q}^{\rm gain}_{\rm heat}}. \quad (24)$$

Generally, the deeper gravitational well of the general relativistic simulations (represented by blue, black, and green lines and points) allows more gravitational binding energy to be released during the accretion phase and results in a higher electron neutrino and electron antineutrino luminosity, which are predominately fueled by accretion, when compared to the Newtonian simulations (red lines). The deeper gravitational well also leads to higher matter temperatures at the neutrinospheres and therefore higher root mean squared energies. This gives larger heating rates and heating efficiencies. The 'case R' effective gravitational potential (labeled as GR1D GREP-R; green curve) overestimates the correction to the gravitational potential and gives even higher luminosities and energies (Marek et al. 2006). Important for our discussion is that our 'case R' results (green lines) closely match the 'case R' results from the Vertex code (Liebendörfer et al. 2005) This agreement, along with the effective potential test cases in Appendix A, gives us confidence in our effective potential implementation. The improved effective potential presented by Marek et al. (2006), (their 'case A'), comes much closer to reproducing the neutrino luminosities, and matches very closely the root mean squared energies, of the full GR codes *Agile*-Boltztran and GR1D.

The differences that are seen between the GR1D and GR1D-GREP collapse results (e.g. GR1D gives $\sim 2-3\%$ lower electron-type neutrino luminosities, $\sim 5\%$ lower heavy-lepton luminosities, and root mean squared energies within $\sim 1\%$; but $M_{\rm gain}$, heating rates, and $\eta_{\rm heat}$ all lower by $\sim 10-15\%$), are due to the differences between the Newtonian hydrodynamics + GR effective potential gravity and GR hydrodynamics + GR gravity. The differences in the neutrino heating quantities are relatively large. The heating quantities are non-linear in the sense that an increased neutrino luminosity or mean squared energy not only increases the specific heating rate, but also increases the size of the region that undergoes net heating. This gives even higher total heating rates. While this is worrisome, noting the heating rates seen in *Agile*-Boltztran (blue points), and in the work of Müller et al. (2012b), reassure us that the heating rates we observe in our effective potential simulations are not overestimated, and in fact, similar to those found in the literature.

The differences in the results of the FLASH simulations and the GR1D-GREP simulations are the result of the neglected transport terms in FLASH: *1)* inelastic neutrino-electron scattering, *2)* energy-group coupling, and *3)* velocity dependence. Understanding these differences is important in order to justify these assumptions for our multidimensional work and quantify the effect they may have. We comment on each of these assumptions individually below.

Assumption 1: Inelastic neutrino-electron scattering (NES). NES plays a dominant role during the collapse phase where down-scattering of neutrinos allows a faster deleptonization of the core. Along with a proper treatment of neutrino advection via velocity terms, it is important in setting the structure of the inner core at the time of bounce (Bruenn 1985). All our simulations include this important role of NES as the evolution of the collapse phase is always performed in GR1D, which includes NES. After bounce, the main influence of NES is to down-scatter heavy-lepton neutrinos (Thompson et al. 2003). Electron-type neutrino and antineutrinos are emitted at too low of a density, and have charged-current interactions that overwhelm NES. In Fig. 1, we see the consequence of ignoring NES in the root mean squared heavy-lepton neutrino energies and luminosities. The FLASH simulations, both GREP and NW, have on average 4-6 MeV higher ($\sim 25\%$) heavy-lepton ν_x root mean squared energy and $2-3\times10^{51}$ erg s^{-1} ($\sim 10\%$) higher luminosities, consistent with the observations of Thompson et al. (2003). However, within the time simulated, the different ν_x luminosities or the extra heating at higher densities supplied by inelastic NES does not have an influence on the electron-type neutrino luminosities or energies, and therefore the heating quantities. For the purposes of neutrino signal prediction, this assumption is quite severe, however there is little effect on the early core-collapse supernova dynamics.

Assumption 2: Energy-group coupling. The neutrino moment evolution equations shown in Eq. 7 - Eq. 11 neglect the transport of neutrinos between energy bins. One important role these terms play in GR transport is the red-shifting of the neutrino spectrum as the neutrinos leave the gravitational well. For the FLASH simulations, the addition of the $\alpha F_i \partial_i \phi$ and similar terms on the right hand side of these equations account for the energy and momentum loss from gravitational redshift, but the shifting of the spectrum is not present because of our neglect of the energy-group coupling terms. As a consequence, there is little difference between the electron type neutrino luminosities in FLASH and GR1D-GREP ($\sim 1\%$ higher in FLASH) but a larger difference in the emitted root mean square energies (FLASH is higher than GR1D-GREP by $\sim$2.5% and $\sim$6% for ν_e and $\bar{\nu}_e$, respectively, at 100 ms after bounce). Electron antineutrinos are affected more because they originate deeper in the gravitational well and therefore undergo more red-shifting. As a note, for s15WW95, the deviation of the general relativistic lapse from 1, which represents the extent to which neutrino will redshift as they escape the gravitational well is $\sim$0.05 at the neutrinospheres ($\sim$35-50 km), consistent with the difference seen here. The higher electron-type neutrino root mean square energies increases the neutrino heating in the gain region. In all heating related quantities we see $\sim 8\%$ higher values in FLASH compared to GR1D-GREP. Gravitational redshift is not included in the Newtonian calculations, therefore these particular differences do not show up for the red lines in the various panels of Fig. 1.

Assumption 3: Velocity-dependent transport terms. Similar to NES, velocity dependent terms are very important during the collapse phase since neutrinos are trapped in matter that is moving at a significant velocity. However, after bounce, the matter velocities everywhere interior to the shock are very small. For example, at 100 ms after bounce the velocity throughout the gain region, where the neutrino heating occurs, is $\sim$1% of the speed of light. This magnitude of velocity would translate into velocity dependent corrections to the neutrino heating in the gain region of $\sim$1-3%. Outside of the supernova shock the matter velocities are much higher,

$\sim 10-30\%$ of the speed of light, however, very little emission or absorption is occurring in this matter after bounce.

3.2. *2D Newtonian Results*

We perform a total of seven two dimensional core collapse simulations using Newtonian gravity. For all simulations, we start from profiles taken from GR1D 15 ms after bounce. We perform the analogue to the 1D Newtonian simulations presented in the previous section, using the 15 $M_\odot$ progenitor from Woosley & Weaver (1995) and the LS180 EOS, model s15WW95_LS180. We also perform four simulations of the models introduced in Table 1, s12, s15, s20, and s25 from Woosley & Heger (2007) (WH07). We use our base resolution and the LS220 EOS. As mentioned in §2.1, we assume $l_{\rm max} = 0$ in our multipole gravity solver. We test this assumption here by performing a Newtonian transport simulation with model s12 and with $l_{\rm max} = 24$. Finally, we test our effective potential solver by performing a Newtonian simulation with the s12 progenitor and where the gravity is computed via the algorithm in §2.1, but replacing the differential equations with the Newtonian equivalent. Theoretically, this is precisely the same as the standard monopole term for the gravity, but numerically calculated in a different way. For both of these test simulations we see no differences other than the stochastic behavior of the convection and turbulence.

In Fig. 2, we show a subset of results from our Newtonian simulations. The 2D simulations are not successful. The simulations of the four models from WH07 proceed similarly. In both 1D and 2D, in all four models, the shock initially expands out and reaches $\sim$170 km at $\sim$100 ms after bounce. Only at this time do the 1D and 2D simulations begin to depart from each other as convection begins to strongly develop behind the shock and provide additional pressure support for the supernova shock (Murphy et al. 2013; Couch & Ott 2015). In 1D and 2D the shocks begin to recede. Compositional interfaces reach the shock front at $\sim$250 ms, $\sim$300 ms, and $\sim$500 ms for models s20, s25, and s12, respectively. At these times, especially in models s25 and s20, we see a short phase of shock expansion. The shock expansion is more prominent in 2D than in 1D. However, this is not sufficient to reenergize the shock in these simulations.

A useful diagnostic of proximity to explosion is the ratio of the advection time through the gain region to the time it takes to unbind the gain material through neutrino heating. A ratio of 1 can be thought of as a runaway condition where matter is unbound before it can be advected into the cooling region. Quantitatively we define this ratio via,

$$\frac{\tau_{\rm adv}}{\tau_{\rm heat}} = \frac{M_{\rm gain}/\dot{M}}{|E_{\rm gain}|/\dot{Q}_{\rm heat}}\,. \tag{25}$$

We define the gain region to consist of any grid zone with a net positive change in the internal energy of the matter due to neutrino interactions. $M_{\rm gain}$ is the total mass of those grid zones, $\dot{M}$ is the accretion rate measured at 500 km, $\dot{Q}_{\rm heat}$ is the rate of energy exchange between the neutrino and the matter in the gain region, and $E_{\rm gain} = \sum_{\rm gain} m_i[1/2|v_i|^2 + \epsilon_i + \phi_i]$ is the energy of the matter in the gain region. For the latter, v_i is the matter velocity, ϕ_i is the gravitational potential, and ϵ_i is the specific internal energy of the matter. For consistency with other works, we take the zero point defined in LS220 EOS for ϵ_i. In the top right panel of Fig. 2 we show this quantity for our Newtonian models. For most of the time, the WH07 models we simulate are below $\tau_{\rm adv}/\tau_{\rm heat} \sim 0.5$, and extend up to $\sim$0.6 only during the brief phase of shock expansion following the accretion of a compositional interface.

Qualitatively, model s15WW95_LS180 is similar to the WH07 models, but there are quantitative differences. The radius at which the shock initially stalls is $\sim$10-15 km smaller than the WH07 models. Furthermore, the compositional interface is located at a much lower mass coordinate and accretes through the shock around $\sim$150 ms after bounce. The significant density jump at this interface leads to a large shock expansion, $\sim$30 km in 1D and $\sim$50 km in 2D. Due to this shock expansion the advection timescale increases and $\tau_{\rm adv}/\tau_{\rm heat}$ reaches $\sim$0.6 in 1D and $\sim$0.8 in 2D. This is the closest any Newtonian simulation gets to an explosion, but even for this case, the shock is not revived.

In the center panels of Fig. 2 we show the neutrino luminosities measured at 500 km. From left to right, we show ν_e, $\bar{\nu}_e$, and ν_x luminosities for all five models. Since all five models fail to explode, the mass accretion rate through the shock and into the cooling region is identical between the 1D and 2D simulations. This sets the gravitational binding energy released, and the energy available to be radiated by neutrinos. Around $\sim$100 ms, when the simulations begin to strongly depart from spherical symmetry, the fluid motions behind the shock cause variability in the neutrino luminosities, however, the mean luminosity follows the 1D result. Our ν_x luminosities are not as dramatically influenced by the fluid motions in the gain region as they are emitted from deeper in the cooling region away from the convective motions. Consequently, they show less variability than both ν_e and $\bar{\nu}_e$. However, there is a significant multidimensional effect on the ν_x neutrinos. We see a boost in the ν_x luminosities due to PNS convection. This convection slows the recession of the neutrinosphere, and dredges up heat from deeper in the PNS. This results in an increase in the ν_x luminosity starting around $\sim$300 ms. We give a more detailed discussion of protoneutron star convection, in §4.

3.3. *2D Effective GR Results*

Our simulations using the GR effective potential are qualitatively different than the simulations using Newtonian gravity presented in the previous section. In our simulations using the GR effective potential we achieve runaway supernova shocks in our core collapse simulations for three of the four progenitors models: s15, s20, and s25. We attribute this to the increased heating in the GREP simulations discussed in the context of 1D models presented in §3.1. This increased heating is a result of the more compact protoneutron star configurations afforded by GR gravity. This gives higher electron neutrino and antineutrino luminosities and root mean squared energies. In Fig. 3, we show the evolution of the mean shock radius in our GREP simulations. The top left panel shows the early shock development, while the top center panel shows the shock evolution out to 3000 km. The WH07 simulations start very similar to the pure Newtonian simulations. Initially, the shock radius extends out to $\sim$155 km at $\sim$100 ms, roughly 15 km lower than the Newtonian simulations. As with the Newtonian simulations, the shock begins to recede in both 1D and 2D. However, unlike the Newtonian simulations, neutrino heating behind the shock is strong enough to cause the shock to become reenergized and propagate out in three of the four

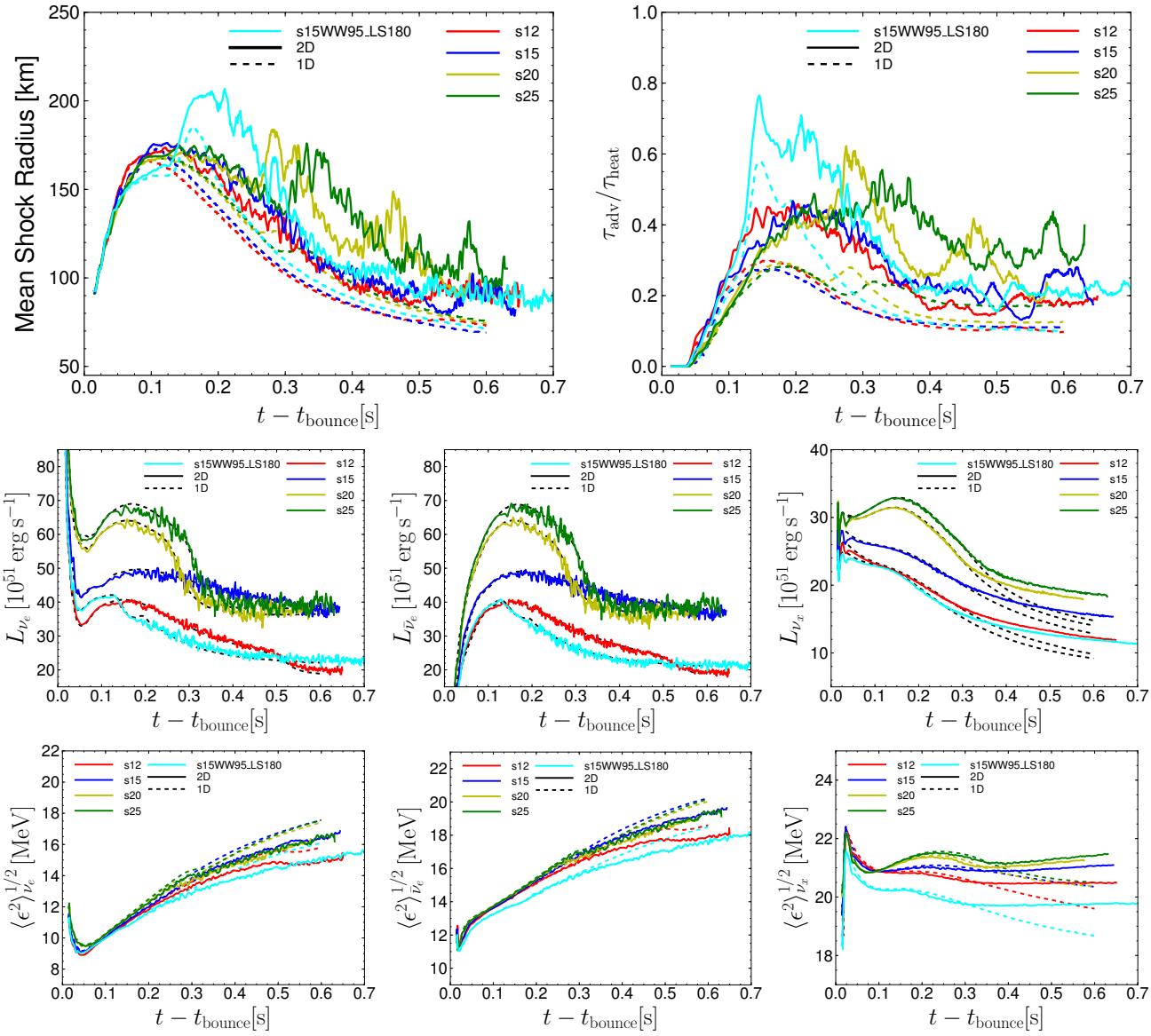

Figure 2. Simulation results from 1D and 2D core collapse using Newtonian gravity in five models. We show the time evolution of the mean shock radius (top left); $\tau_{\rm adv}/\tau_{\rm heat}$ (top right); and ν_e, $\bar{\nu}_e$, and ν_x luminosity (root mean squared energy) in the center (bottom) left, middle, and right plots, respectively. Solid lines are from 2D simulations, while dashed lines are from 1D simulations. Models s12, s15, s20, and s25 are performed with the LS220 EOS, model s15WW95 uses the LS180 EOS for comparison purposes. To reduce the scatter, we average $\tau_{\rm adv}/\tau_{\rm heat}$ over a 5 ms window.

WH07 models. For s20 and s25, this reversal occurs between 200 and 300 ms after bounce, roughly when the compositional interface associated with the silicon-oxygen interface accretes through the shock. The shock revival in model s15 occurs much later, ∼600 ms. The times at which the mean shock radii reach 500 km are ∼737 ms, ∼396 ms, and ∼350ms for models s15, s20, and s25, respectively. These values are listed in Table 1. Like the set of Newtonian simulations, the s15WW95_LS180 model is markedly different than the WH07 models, the shock radius stagnates at a lower radius, ∼140 km, then extends to a much larger radius (∼180 km) after the compositional interface accretes through the shock at ∼150 ms before ultimately receding and failing to be reenergized.

In Fig. 3, we show the ratio of the advection time through the gain region to the time it takes to unbind the matter in the gain region due to neutrino heating, $\tau_{\rm adv}/\tau_{\rm heat}$, defined in Eq. 25. In models s15, s20, and s25, $\tau_{\rm adv}/\tau_{\rm heat}$ surpasses unity at ∼650 ms, ∼270 ms, and ∼250 ms, which corresponds to the time when the mean shock radius is starting its outward propagation. The s12 and s15WW95_LS180 models never surpass the value of unity, these models do not explode. For the exploding models, large, late-time asymmetries in the explosion morphology lead to value of $\tau_{\rm adv}/\tau_{\rm heat}$ less than unity. This is due to the break down of the underlying assumptions of Eq. 25, which is technically only valid for spherical flows.

The center row of Fig. 3 shows the luminosity of each of the three neutrino species. Prior to explosion, or for the entire evolution for models s12 and s15WW95_LS180, the neutrino luminosities closely follow the 1D simulation. This was the case for the Newtonian models as well and, as explained in the previous section, is because the neutrino luminosity being emitted in simulations with stalled or failing supernova shocks is set by the accretion rate, which is the same in both

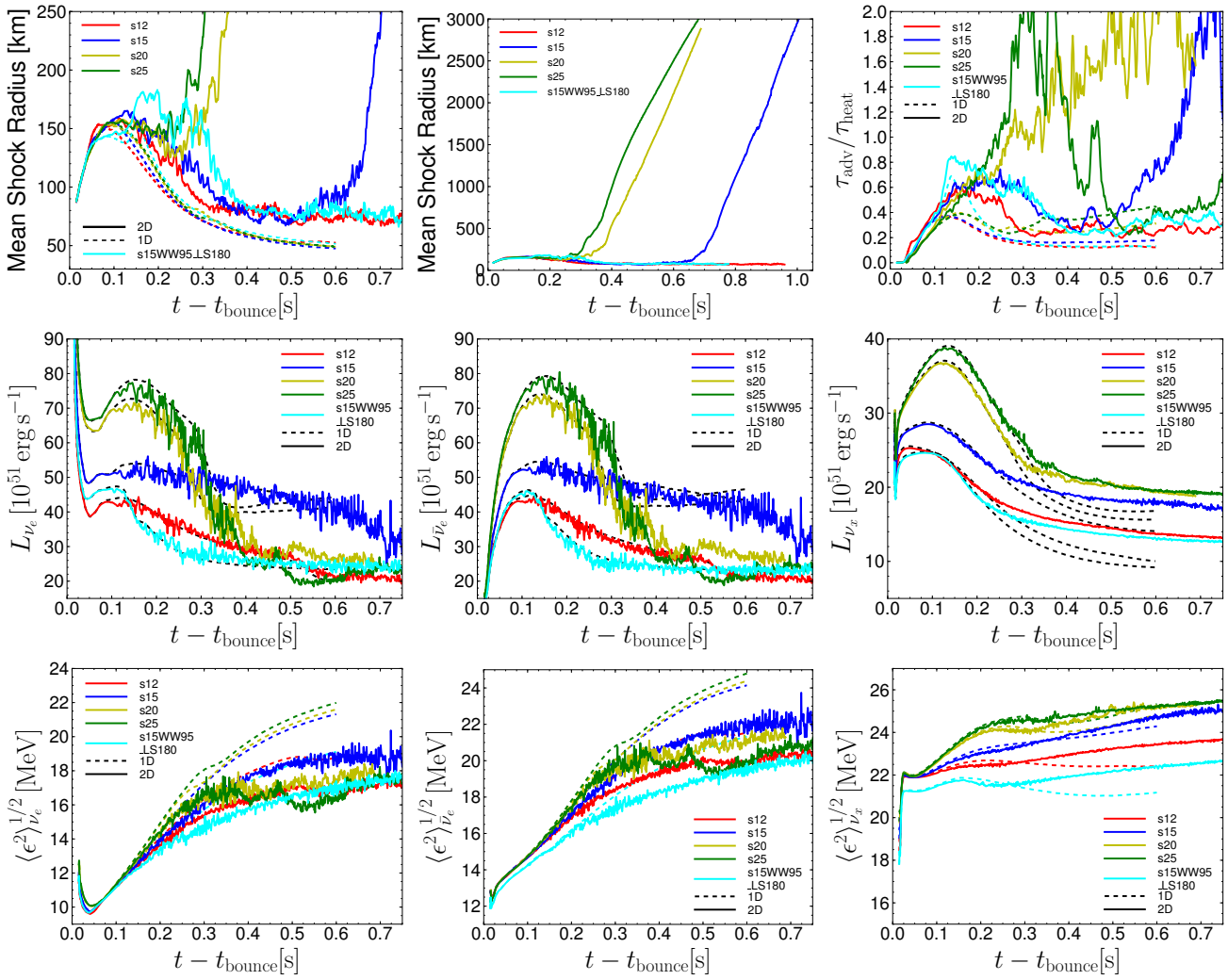

Figure 3. Simulation results from 1D and 2D core collapse using GR effective gravity in five models. We show the time evolution of the mean shock radius (top left and top center); $\tau_{\rm adv}/\tau_{\rm heat}$ (top right); and ν_e, $\bar{\nu}_e$, and ν_x luminosity (root mean squared energy) in the center (bottom) left, middle, and right plots, respectively. Solid lines are from 2D simulations, while dashed lines are from 1D simulations. Models s12, s15, s20, and s25 are performed with the LS220 EOS, model s15WW95 uses the LS180 EOS for comparison purposes. To reduce the scatter, we average $\tau_{\rm adv}/\tau_{\rm heat}$ over a 5 ms window.

1D and 2D. The situation changes after the explosion sets in. After this time, accreted matter is no longer able to settle into the cooling region since it is being heated by neutrinos and ejected. As a result, the released gravitational binding energy is not being converted into neutrino luminosity. The consequence is that the post-explosion neutrino luminosity in 2D is lower than the neutrino luminosity determined in the 1D simulation at the same time. As was the case for the Newtonian simulations, we see the impact of protoneutron star convection on the ν_x luminosities.

In the top panel of Fig. 4, we show the early development of the diagnostic explosion energy (Buras et al. 2006; Bruenn et al. 2013; Melson et al. 2015),

$$E^{\rm diag}_{\rm exp} = \int_{\mathcal{V}} d\mathcal{V}\rho[1/2|v|^2+(\epsilon-\epsilon_0)+\phi]_{>0}\,, \qquad (26)$$

where the volume integral is over all zones where the integrand is positive. ϕ is the gravitational potential energy, ϵ is the specific internal energy and ϵ_0 is the specific internal energy of matter with the same density and Y_e, but $T = 0$. This roughly accounts for the energy that will be released into kinetic energy as the matter cools and the free nucleons recombine into alpha particles, and later nuclei. To truly determine this energy one must track the evolution to much longer times and do a proper treatment of nucleosynthesis, something we are not capable of doing with our current infrastructure. We also note that this diagnostic explosion energy does not account for the binding energy of the material outside the shock (i.e, the "overburden"). Our explosion energies are quite small compared to the results of Bruenn et al. (2013), and more along the lines predicted from other successful explosions in two and three dimensions (Hanke et al. 2012; Melson et al. 2015; Müller et al. 2012b; Suwa et al. 2010; Pan et al. 2015; Suwa et al. 2014). In our simulations, along with the weak explosions comes continued accretion after the explosion sets in. We show this in the bottom panel of Fig. 4, where we show the PNS mass (PNS defined as the region with a matter density of at least 10^{11} g cm^{-3}) in 2D (solid lines) and 1D (dashed lines). The simulations which do not produce explosions have similar PNS masses in 1D and 2D. For the simulations that explode, the growth of the PNS mass slows after the explosion sets in, but is not zero in any model at the latest times simulated. Finally we note that the explosions are essentially unipolar with

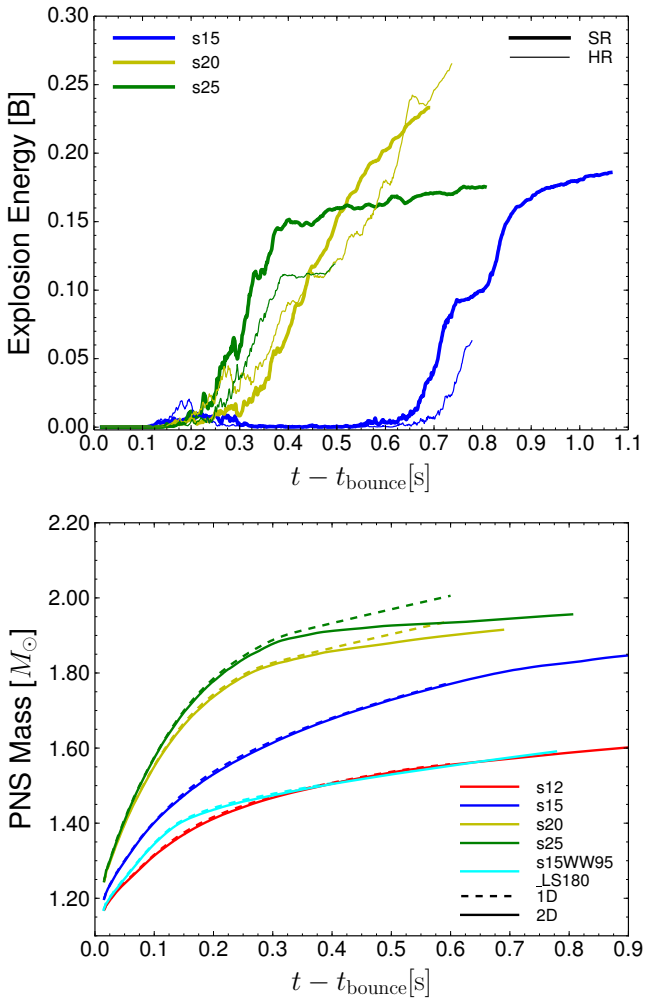

Figure 4. Diagnostic explosion energies for exploding models determined via Eq. 26 (top panel) and cumulative PNS baryonic mass (bottom panel). The explosion energy estimate includes an estimate of the nuclear recombination energy, but does not include the binding energy of the overlying star. As thin lines, we show the development of the explosion energies from higher resolution models. The PNS is defined as the region with matter densities larger than 10^{11} g cm^{-3}. Solid lines denote the mass from 2D simulations with dashed lines are from 1D simulations.

accretion occurring along the opposite pole. We show graphical snapshots of our three exploding models in Fig. 5 at a time determined by when the maximum shock radius reaches 5000 km, corresponding to 962 ms, 659 ms, and 734 ms after bounce for models s15, s20, and s25, respectively.

3.3.1. *Resolution Study*

We also simulate core collapse in models s12, s15, s20, and s25 with an increased resolution and GREP gravity. Our finest level of refinement in our high resolution simulations has cells with a side length of 325 m (compared to our standard resolution of 488 m). This increases the effective angular ($\Delta r/r$) resolution accordingly, from at least 0.5 degrees, to at least 0.34 degrees. In 2D, this gives roughly twice the number of computational zones, and a ∼33% smaller time step. The qualitative results remain the same in all four simulations. Our higher resolution simulations of models s15, s20, and s25 still develop explosions. The explosion times are slightly different. For model s15, the time when the mean shock radius reaches 500 km is ∼781 ms, or ∼44 ms later than the lower resolution run. For model s20, the higher resolution simulation gives a postbounce time when of the mean shock reaches 500 km of ∼381 ms, or ∼15 ms earlier than the lower resolution simulation. Finally, for the s25 simulation, mean shock radius reaches 500 km at a postbounce time of ∼355 ms, ∼5 ms later than the standard resolution. Our high resolution simulation of model s12 also shows the same behavior that the lower resolution model shows, it fails to explode. The development of the explosion energies for the successful models (see thin lines in Fig. 4) are similar between resolutions. For model s15, the initial rise of the diagnostic explosion energy is delayed ∼44 ms due to the later explosion time. The shock expansion in model s20 (s25) begins earlier (later) in the higher resolution model, which we attribute this behavior to the stochastic nature of the postshock convective motions. All diagnostic quantities remain essentially identical between resolutions.

4. DISCUSSION

4.1. *GR vs Newtonian Gravity*

From the results presented in the last section, it is clear that the approximation of Newtonian gravity gives less favorable conditions for a successful core-collapse supernova explosion than the more realistic GR treatment. Even though we do not include fully GR gravity and hydrodynamics, the test results of §3.1, and the comparisons to the previous work of Liebendörfer et al. (2005); Marek et al. (2006) convince us that using an effective GR potential allows us to capture the important aspects of GR for modeling core-collapse supernovae. Most importantly, the 1D results of §3.1 show that GR gravity leads to higher neutrino luminosities, and higher root mean squared energies which directly follow from a more compact protoneutron star structure. The neutrino mechanism relies on the capture of neutrinos emitted from the cooling region into the gain region. This capture is greater with higher luminosities, and more efficient with higher neutrino energies. However, in 1D, the added benefits of GR do not lead to successful explosions as has been previously demonstrated (Liebendörfer et al. 2001). This trend of increased heating and higher heating efficiencies carries over to 2D, which we demonstrate in Fig. 6. In this figure, we show the net heating rate in the gain region (top) as well as the heating efficiency (middle; Eq. 24), for the four WH07 models and the s15WW95_LS180 model using the GR effective potential gravity (solid lines) and Newtonian gravity (dashed lines). In all models, both the heating rate and the heating efficiency are larger in the simulations using the GR effective potential, by ∼20-30% between 100 ms and 200 ms after bounce. Furthermore, the appearance of the gain region occurs sooner for the GREP models by ∼20 ms. The increased heating in the 2D simulations using GR gravity is enough to drive an explosion in three of the five models simulated. These three GR models have the highest net heating rate and the highest heating efficiency of all 10 Newtonian and GR models simulated.

The GR models also show signs of increased susceptibility to, and presence of, convective activity in the gain region compared to the Newtonian models. Disentangling the cause and effect relationship between the increased neutrino heating and the presence of convection is difficult, what is clear is both are stronger in the GR simulations. In Fig. 7, we show

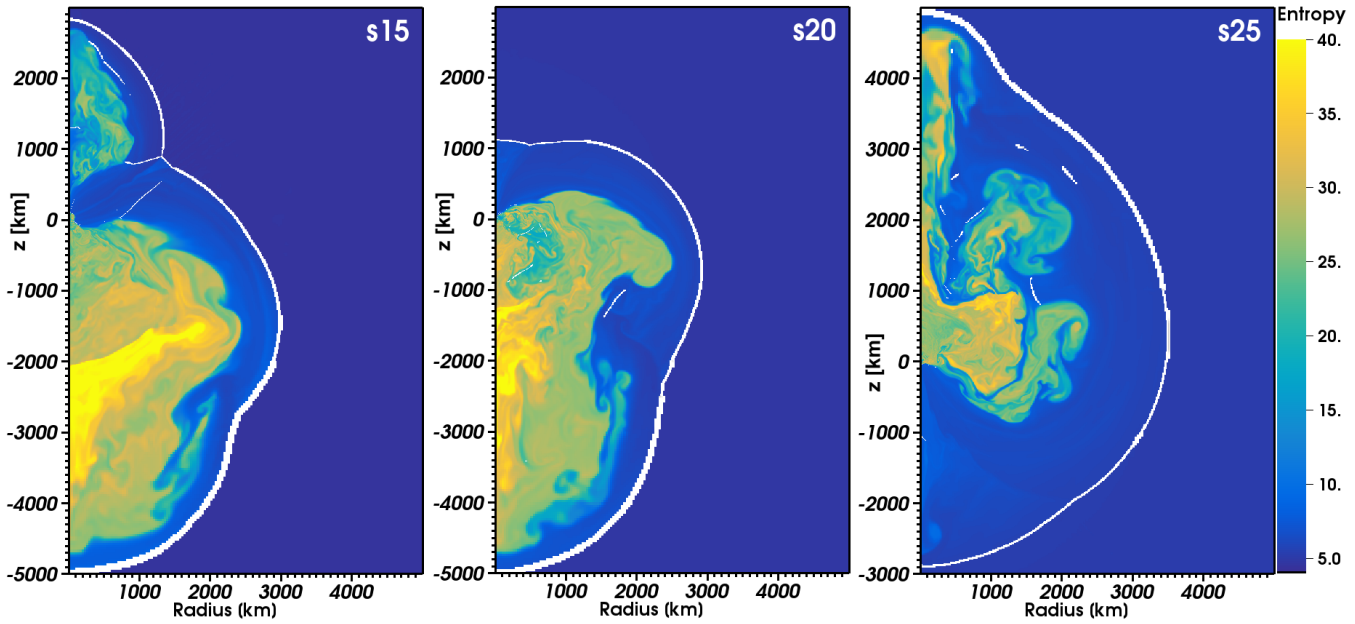

Figure 5. Entropy color plots of exploding models s15, s20, and s25 at 962 ms, 659 ms, and 734 ms after bounce, respectively. These times correspond to when the shock front first reaches 5000 km. The color scale, shown on the right, is the same for all three images. The explosions are strongly unipolar, indicative of weak explosions. White zones correspond to the shock position.

color maps of the Brunt-Väisälä frequency, $\omega_{\rm BV}$, as a function of time and radius for each studied model from WH07, and for both treatments of gravity. For each time slice we angle average the matter properties and using the average radial profile we compute $\omega^2_{\rm BV}$ (Foglizzo et al. 2006),

$$\omega^2_{\rm BV} = \frac{d\phi}{dr}\left(\frac{1}{\gamma}\frac{d\ln P}{dr} - \frac{d\ln\rho}{dr}\right), \quad (27)$$

and take

$$\omega_{\rm BV} = {\rm sign}(\omega^2_{\rm BV})\sqrt{|\omega^2_{\rm BV}|}, \quad (28)$$

where $d\phi/dr$ is the radial gradient of the gravitational potential and γ is the adiabatic index. Positive values of $\omega_{\rm BV}$ (blue) denote convectively stable regions while negative values (red) denote convectively unstable regions. On each graph we also show the mean and maximum shock radius as green and magenta lines, respectively, and the average gain radius as a red line. We note several important results from these graphs.

In all models, the first sign of convectively unstable regions occurs soon after bounce between the gain radius and the shock. However, due to the high advection rate of material through the shock, the material does not become convection-dominated until $\sim$ 100 ms after bounce. In general, the GREP runs in Fig. 7 show darker hues of red, signaling that the matter is more susceptible to convection (i.e., the convective growth rate is faster). We can see both of these points by looking at the non-radial kinetic energy in the gain region for each Newtonian and GREP model, shown in the bottom panel of Fig. 6. GREP models have more total lateral kinetic energy even though the mass of the gain region is typically smaller than the Newtonian models (see §3.1; this difference carries over to the WH07 models and 2D as well). This implies an even larger disparity between the specific lateral kinetic energies. In both Newtonian and GREP gravity simulations, there is no significant lateral kinetic energy until $\sim$ 100 ms after bounce when convective seeds can finally grow fast enough before getting advected into the cooling region below the gain radius. Similar to the net heating, the rise of convective motions is slightly earlier in the GREP models.

Fig. 7 also shows signs of PNS convection. PNS convection is seen in all our of 2D models at a radius of $\sim$20 km. There are signs of convective instability in the core starting as early as $\sim$100 ms, but strong instabilities do not develop until $\sim$200-250 ms in all models. The strength of this instability is higher in more massive progenitors and in GREP gravity. The onset of PNS convection also occurs earlier (up to $\sim$50 ms) in the GREP simulations. This convection has a quantitative effect on the neutrinos being emitted in our 2D simulations. PNS convection prevents the neutrinospheres from receding as they do in the corresponding 1D simulations. This predominantly impacts the heavy-lepton neutrinos as they are emitted from the deepest regions of the star, closest to the PNS convection zone. The increased neutrinosphere radius gives a larger ν_x luminosity as can be seen in Fig. 2 and Fig. 3.

4.1.1. *Comparison to Literature: Newtonian Gravity*

Many aspects of our results compare quite well to the Newtonian results of Dolence et al. (2015). Dolence et al. (2015) use the same progenitor models, the same neutrino microphysics (based on Bruenn (1985); Burrows et al. (2006)), and also a truly multidimensional neutrino transport scheme, albeit MGFLD. Matching our simulations, none of the 2D simulations in Dolence et al. (2015) explode. Comparison of $\tau_{\rm adv}/\tau_{\rm heat}$ show good agreement. At $\sim$200 ms, $\tau_{\rm adv}/\tau_{\rm heat} \sim$ 0.45 in both simulation sets and for all four models. The ratio increases when the compositional interfaces accrete through the shock at $\sim$300 ms after bounce in models s20 and s25. Furthermore, our heating efficiencies (see Fig. 6) at $\sim$200 ms after bounce are between 0.06 and 0.08, similar to Dolence et al. (2015). It is important to remember that these simulations do not use the same equation of state, and therefore a direct comparison is potentially flawed. Dolence et al. (2015) have lower luminosities and root mean squared energies when compared to the results here. This is likely due to use of the H.

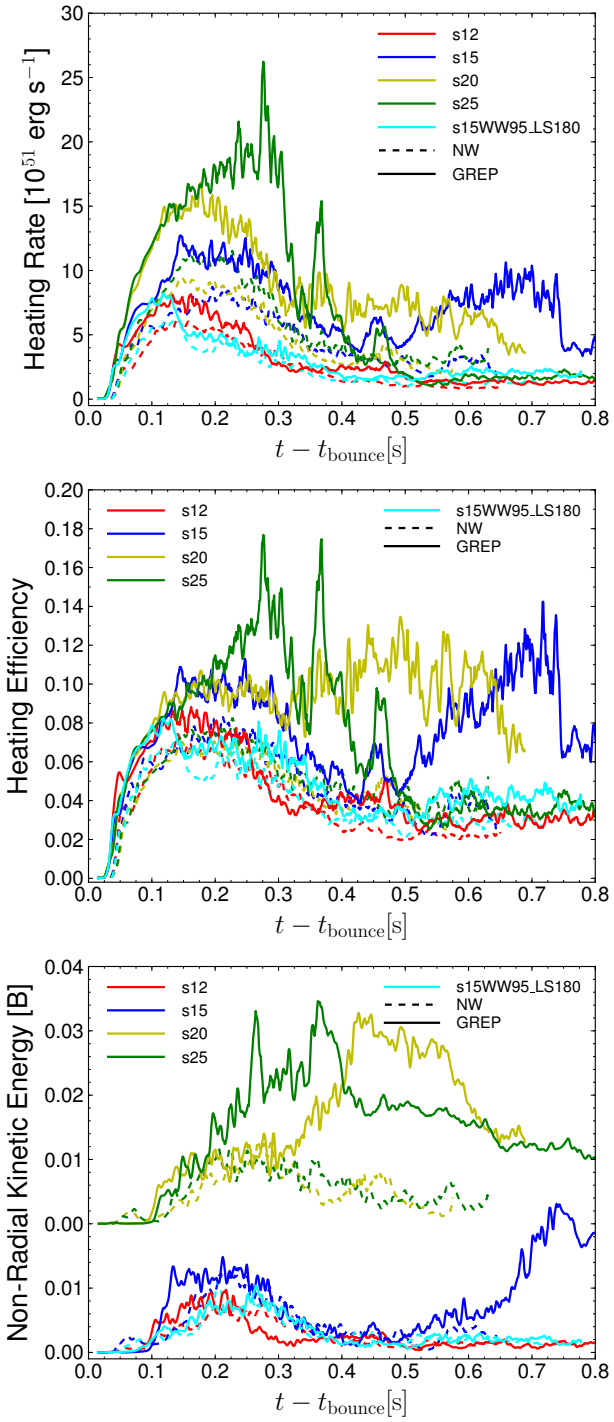

Figure 6. Neutrino heating metrics for 2D simulations with both GR effective potential gravity and Newtonian gravity. We show the net heating (top panel), the heating efficiency (middle panel), and non-radial kinetic energies in the gain region (bottom panel) for each of the four WH07 models and model s15WW95_LS180 used in this study. Simulations with Newtonian gravity are shown as dashed lines while the GR effective potential simulations are solid lines. For the bottom panel, models s20 and s25 are shifted up for clarity. All curves are averaged over 5ms to reduce noise.

Shen EOS, which gives larger neutrinosphere radii, and hence lower luminosities and root mean squared energies, which will directly impact the heating rates and efficiencies.

A stark difference between this work and the work of Dolence et al. (2015) is the shock radius evolution. In the simulations of Dolence et al. (2015) the 2D simulations quickly (∼5 ms after bounce) diverge from the 1D equivalent. The authors' explanation is prompt convection soon after bounce in concert with the aspherical, cylindrical geometry. We also use cylindrical geometry, but since we start our simulations at ∼15 ms after bounce, we miss some potential prompt convection within a few ms of core bounce. We have done a test in 2D where we use our radiation transport from the onset of collapse through the collapse phase and through bounce. We do see initial prompt convection, but not enough to drive the shock radius out a significant distance (only ∼10 km further). We do caution that this test simulation does not have the full neutrino transport necessary for collapse, hence, the inner core has a small mass (central $Y_e \sim 0.2$) and, furthermore, neutrinos are not advected with the fluid flow, which may be relevant for prompt convection right after bounce when optically thick material is moving with significant non-zero velocities. This caution was the motivation for us using the full transport physics of `GR1D` for the collapse and early postbounce phase.

Two-dimensional Newtonian simulations of these models are also presented in Suwa et al. (2014) using IDSA for neutrino transport. There, the LS220 EOS is used. They observe an early explosion in a few models, including s12, and failure in the majority of the rest. One issue preventing a detailed comparison is that Suwa et al. (2014) ignore heavy-lepton neutrinos in their simulations. It is likely the case that this prevents the protoneutron star from cooling and causes the shock to initially stall at ∼ 240 km and hover around ∼200 km in failed models. Pan et al. (2015) also perform Newtonian axisymmetric simulations of core collapse using IDSA for neutrino transport. Although they use the same version of `FLASH` for their hydrodynamics, which removes some differences between the simulation setup, they simulate different progenitor models and use different equations of state. This makes direct comparisons very difficult. However, they find explosions for all progenitors simulated: 11 $M_\odot$, 15 $M_\odot$, 21 $M_\odot$, and 27 $M_\odot$ models from Woosley et al. (2002).

4.2. *Comparison to Literature: GR Gravity*

Our GREP results compare quite well to the Hanke (2014) results. Below, we note several key similarities and differences.

Explosion times: In Table 1 we present the postbounce times when the shock reaches 400 km in the simulation of Hanke (2014). They are ∼620 ms, ∼320 ms and ∼400 ms for models s15, s20, and s25, respectively. These are all within ∼100 ms of our results. Unlike Hanke (2014), where a late explosion at ∼790 ms was seen for model s12, we do not see an explosion before ∼1 s, when our simulation was stopped.

Shock evolution: The evolution of the mean shock radius is also qualitatively similar. The initial stalling radius in our simulations is ∼155 km compared to ∼160 km in Hanke (2014). After this, there is a period of shock recession before the ultimate shock expansion. However, the simulations of Hanke (2014) have a much more pronounced shock recession. This may stem from the differences in the neutrino interactions used. Hanke (2014) use inelastic neutrino-nucleon scattering and absorption opacities from Burrows & Sawyer (1998, 1999) whereas we use simpler elastic rates from Bruenn (1985). They use microphysical electron capture rates on heavy nuclei for the collapse phase instead of the

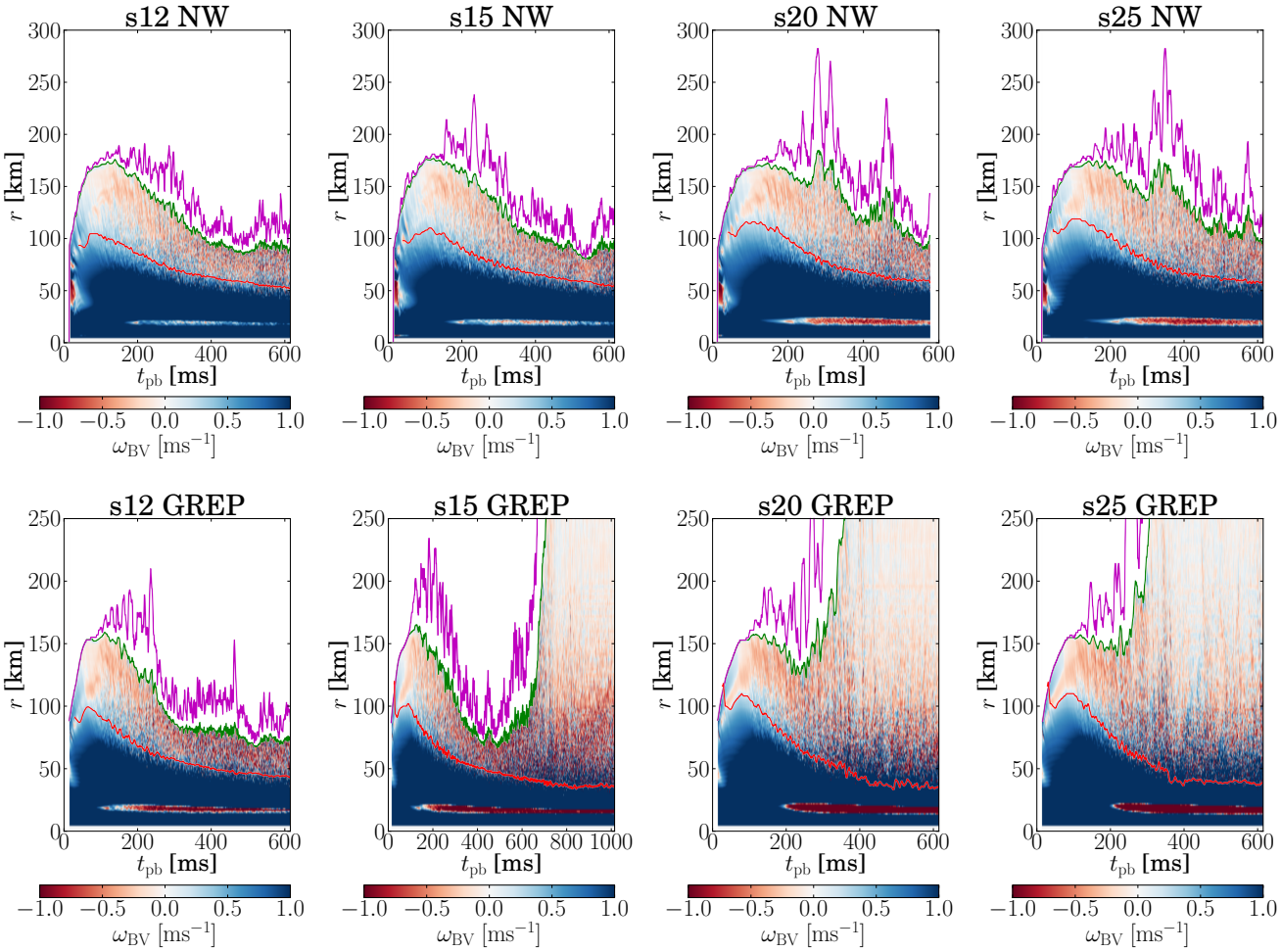

Figure 7. Color maps of the Brunt-Väisälä frequency for each Newtonian and GR effective potential model as a function of time and radius. Red colors denote convectively unstable regions while blue regions are convectively stable. Shown as green, magenta, and red lines are the mean shock radius, maximum shock radius, and gain radius, respectively. We mask out the color map in between these regions.

approximate form from Bruenn (1985) implemented here. Finally, Hanke (2014) include neutrino-neutrino pair scattering and annihilation (to other neutrino pairs) as additional pair-processes. One important consequence of these improved opacities is the more efficient cooling of the PNS which gives higher ν_x luminosities and faster contraction and as a consequence.

Convective Motions: A potentially important difference between our simulation results and the simulations of Hanke (2014) is the evolution of the non-radial kinetic energies in the gain region which is indicative of increased convective activity. Our 2D simulations, both GREP and Newtonian, have $\sim 10^{49}$ erg of lateral kinetic energy in the gain region at ~150-250 ms after bounce (see Fig. 6), roughly twice the value observed for a different set of progenitors in Hanke (2014). This may be a consequence of our cylindrical grid which imposes non-spherical perturbations (i.e. convective seeds) on our fluid flow. This sign of stronger convective motions behind the shock could be bringing our simulations closer to explosion (Couch & Ott 2013; Müller & Janka 2015). Additionally, since we ignore the red-shifting of the neutrino energy spectrum as it climbs out of the gravitational well, our heating is overestimated (see §3.1). This could also give stronger neutrino-driven convection and larger non-radial kinetic energies.

Neutrino transport: Our neutrino transport is fully multidimensional, while the neutrino transport in Hanke (2014) uses the ray-by-ray+ approximation where lateral transport of neutrinos is neglected in the low density region directly behind the shock. This approximation has not been rigorously tested for dynamical simulations (although see Sumiyoshi et al. 2015 for a hydrostatic comparison of ray-by-ray to truly multidimensional transport) which requires holding everything else fixed to eliminate other sources of differences such as numerical methods, initial conditions, input physics, etc.

Given these lingering differences between our simulations and those of Hanke (2014), a comparison with even closer underlying physics is warranted. Although we find it quite encouraging that we find remarkably close agreement, even with the differences between our simulation codes and simulation techniques.

In contrast, our results are in qualitative disagreement with the results of Bruenn et al. (2013, 2014) (labeled here as Bruenn *et al.*). At 100 ms, all four models in Bruenn *et al.* stall at a radius of ~200 km. However, after the shock stalls it continues to slowly move out in radius until it ultimately

begins to runaway. There is no period of shock recession in any model. We note, however, an updated 2D simulation in Lentz et al. (2015) of model s15 gives a stall radius of ∼175 km, there is still no recession of the shock front in this updated simulation. We can also directly compare neutrino quantities and heating rates with the results in Bruenn *et al*. The neutrino luminosities predicted from both sets of simulations agree within ∼5% (this difference is in part due to the fact that Bruenn *et al.* measure their quantities in the co-moving frame at 1000 km where the fluid velocities are $\sim 0.03\,c$). The root mean squared energies (bottom panels of Fig. 3) show a larger difference, Bruenn *et al.* predict neutrino energies up to ∼ 20% larger than our results at ∼100 ms after bounce, this difference cannot be explained by the difference between the co-moving frame measurements alone, but could be due to differences in the neutrino interactions (which include some of the improved rates included in Hanke (2014) listed above, but not the neutrino-neutrino scattering or annihilation to other neutrino pairs) or the neutrino transport (which is MGFLD, a more approximate, one moment transport scheme using the ray-by-ray+ approximation). Roughly, the neutrino heating rates scale with both the electron-type neutrino luminosity and the electron-type mean *squared* neutrino energy, therefore we expect to see the influence of the higher root mean squared energies seen in Bruenn *et al.* reflected in the heating rates. Our GREP simulations have a net heating rate in the gain region at 100 ms after bounce of $\sim$6.5 B s^{-1}, $\sim$7.5 B s^{-1} $\sim$12 B s^{-1}, and $\sim$12 B s^{-1} for models s12, s15, s20, and s25, respectively, while the heating rate in Bruenn *et al.* at the same time are $\sim$9 B s^{-1}, $\sim$13 B s^{-1}, $\sim$20 B s^{-1}, and $\sim$20 B s^{-1}, for models s12, s15, s20, and s25, respectively (the heating rate at 100 ms after bounce in the updated 2D simulation of model s15 in Lentz et al. (2015) is 9 B s^{-1}). The heating rates seen in the Bruenn *et al.* simulations are roughly ∼50% higher than ours. This large discrepancy at such an early postbounce time warrants further investigation beyond comparison of literature results.

Finally, we note that the heating efficiency of successful models is significantly less than the heating efficiency one would predict was required for an explosion in 1D. For example, O'Connor & Ott (2011) predicts a critical heating efficiency of 0.172, 0.176, and 0.185 for models s15, s20, and s25. The success of these models in our simulations is not due solely to the increase in neutrino heating as a result of multidimensional instabilities, rather the instabilities themselves are directly contributing to success of the explosion (Couch & Ott 2015). Our results, while only consisting of four models, are inconsistent with the 1D parameterized model predictions of success/failure from Ertl et al. (2015): our exploding models are predicted to fail and our failed model is predicted to succeed. The ultimate predictive power of 1D parameterized explosion models like these must be further tested (or calibrated) with multidimensional models.

5. CONCLUSION

The study of core-collapse supernovae is an exceedingly multi-physics problem. If anything, decades of research into the core-collapse supernova central engine has shown that in order to create realistic simulations of these astrophysical phenomena we need to include all of the important underlying physics. This includes, but is of course not limited to, the nuclear equation of state, neutrino transport and neutrino interactions, general relativistic gravity, realistic progenitor models, resolved multidimensional (3D) magnetohydrodynamics, and more. In this paper we have extended the capabilities of the `FLASH` simulation package to now include an effective treatment of general relativistic gravity and a multispecies, multigroup, multidimensional neutrino radiation transport solver. Both of these new implementations are designed for application to the core-collapse supernova problem.

We have tested our GR implementation of gravity and our neutrino transport solver with several classic test problems, including an unstable TOV migration test (in both 1D and 2D), and the M1 shadow test. Furthermore, we perform the benchmark core-collapse test case for GR neutrino radiation transport + hydrodynamics from Liebendörfer et al. (2005) which uses a base set of neutrino interactions based on Bruenn (1985), the LS180 nuclear EOS from Lattimer & Swesty (1991), and the $15M_{\odot}$ progenitor from Woosley & Weaver (1995). Our results closely match those of other neutrino transport methods. We critically assess and make clear the impact of the approximations in our neutrino transport scheme with this comparison.

Extending our simulations to axisymmetry, we study core collapse in four progenitors from Woosley & Heger (2007) with both Newtonian and GR gravity for at least ∼600 ms after bounce. While the benefits that a general relativistic treatment of gravity can have for the core-collapse supernova problem have been discussed before, ours is the first study to systematically explore the differences between Newtonian and GR gravity in multiple dimensions and across several updated progenitor models. Our results clearly and unambiguously show that GR gravity significantly aids the neutrino mechanism in reenergizing the stalled supernova shock formed in the core collapse of massive stars. We obtain explosions in three of four progenitor models from Woosley & Heger (2007) when using general relativistic gravity, while all four models fail to explode when using Newtonian gravity. Consistently in the literature are complicated multi-physics simulations of core-collapse supernova with sophisticated neutrino treatments but Newtonian gravity. The results presented here show that the approximation of Newtonian gravity can be quite detrimental in the context of core-collapse supernova explosions and should be relaxed if accurate results are sought.

Our results match, in several ways, other multidimensional, energy-dependent neutrino radiation transport simulations of core-collapse supernovae including the Newtonian gravity simulations of Dolence et al. (2015) and the GR gravity simulations of Hanke (2014). However, differences still exist between the results of these works and the work present here. This could be due to differences in the neutrino and nuclear microphysics, neutrino transport methods, and/or numerical setups. We find qualitative differences between our work and the work of Bruenn et al. (2013, 2014), which again, could be due to any of potential differences listed above. However, we particularly note significant differences in the amount of the neutrino heating present during the early postbounce phase. A close comparison of methods, input physics, and results is warranted to resolve these differences.

ACKNOWLEDGEMENTS

The authors acknowledge fruitful conversations with F. Foucart, J. A. Harris, R. Hix, H. T. Janka, E. Lentz, O. E. B. Messer, C. D. Ott, L. F. Roberts. Computations were performed on the Zwicky cluster at Caltech, which is supported by the Sherman Fairchild Foundation and by NSF award PHY-0960291. Computations were also performed on the gpc supercomputer at the SciNet HPC Consortium. SciNet is funded by: the Canada Foundation for Innovation under the auspices of Compute Canada; the Government of Ontario; Ontario Research Fund - Research Excellence; and the University of Toronto (Loken et al. 2010). An award of computer time was provided by the Innovative and Novel Computational Impact on Theory and Experiment (INCITE) program. This research used resources of the Argonne Leadership Computing Facility, which is a DOE Office of Science User Facility supported under Contract DE-AC02-06CH11357. Support for this work was provided by NASA through Hubble Fellowship grant #51344.001-A awarded by the Space Telescope Science Institute, which is operated by the Association of Universities for Research in Astronomy, Inc., for NASA, under contract NAS 5-26555.

APPENDIX

NEUTRON STAR MIGRATION TEST

In Fig. 8, we test our GR effective potential implementation via a Tolman-Oppenheimer-Volkoff (TOV) star migration test. We follow the initial conditions from Marek et al. (2006). Our unstable TOV stars follow a $\Gamma = 2$ polytropic EOS, $P = K\rho^{\Gamma}$ with a value of $K = 1.455 \times 10^5$ [cgs]. We take an initial central density of $\rho_c = 4.93 \times 10^{15}\,\mathrm{g\,cm^{-3}}$ and solve the 'case A' modified TOV equations to obtain the equilibrium (but unstable) structure. With simulate 4 ms of evolution in FLASH, in both 1D (red dashed line) and 2D (blue dashed-dotted). We also use the full GR code GR1D to perform the migration test (black solid line), for this full GR test, we use the standard TOV equations to construct the initial profile. In the effective potential tests, the unstable star quickly ($\sim$0.1 ms) starts its migration away from the unstable configuration, and oscillates about the stable configuration. The full GR evolution is slower, especially at the beginning, which we can understand from the time dilation effect in the full GR simulation, the value of the central lapse for this configuration begins at $\sim$0.27, and migrates to $\sim$0.65. Our results compare very well to the 'case A' results and the full GR CoCoNut results of Marek et al. (2006), completing between 7 and 8 oscillation cycles in the first 4 ms of evolution for the effective potentials and $\sim$5 cycles in the full GR case. This convinces us that we have correctly implemented the GR effective potential in both 1D and 2D in FLASH. We have also tested stable TOV star configurations. Using a stable TOV star, with the same EOS and an initial central density of $7.5 \times 10^{14}\,\mathrm{g\,cm^{-3}}$, FLASH maintain this central density over 4 ms to better than 1% in 1D and 0.5% in 2D.

M1 SHADOW TEST

In one-moment transport schemes, like flux-limited diffusion, the flux of energy density is taken to be in the direction of the spatial gradient of the neutrino energy density.

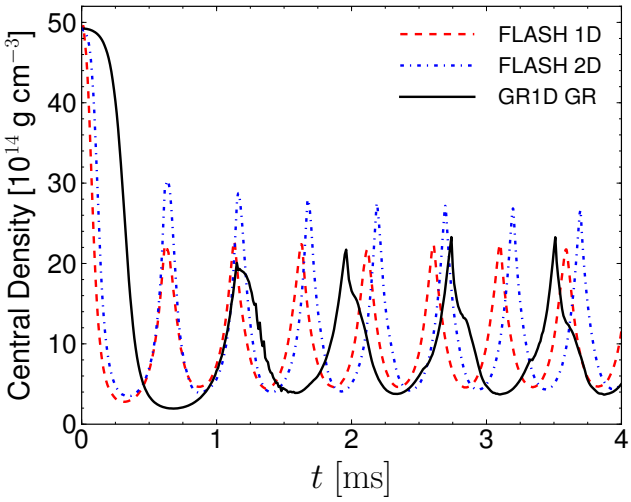

Figure 8. Unstable TOV star migration test. This TOV star migration test is performed in FLASH to test our implementation of the 'case A' GR effective potential from Marek et al. (2006). We present results from a 1D simulation (red dashed line) a 2D simulation (blue dashed-dotted line) and a full GR simulation in GR1D (black solid line). The results compare quite well to those of Marek et al. (2006) and convince us of the correctness of our effective potential implementation.

This works well in the diffusion limit, but in a free streaming regime this assumption works to artificially source neutrino momentum and wash out potentially physical gradients. One of the advantages of a M1-like transport scheme is the ability to maintain the momentum of free streaming neutrinos. The classic test problem to demonstrate this ability of M1 transport is the shadow test. We closely follow the 2D shadow test proposed in Just et al. (2015), with the exception that we employ axisymmetry and use cylindrical coordinates whereas Just et al. (2015) perform their shadow test in genuine 2D Cartesian coordinates, apart from a geometric factor of r, these setups are identical. At the origin, within a spherical radius of $r_s = 1.5$, we have a spherical emission source with an absorption opacity of

$$\kappa_a = 10 \exp[-(4r/r_s)^2], \tag{B1}$$

and an emissivity with an arbitrary normalization. Along the radial direction, a distance of 8 from the central source, we place a purely absorbing ($\kappa_a = 10$) circle (which corresponds to a torus under axisymmetry) with radius of 2. The grid extends to +12 in the radial direction and ± 5 along the symmetry axis. The grid resolution is 0.05. For this test we do not use any mesh refinement, a side effect of this is that we have free streaming radiation on the finest resolution of our grid, our first order method for the explicit flux calculation does poorly unless we lower the CFL factor from 0.4 to 0.2, which we do for this test. We do not encounter this issue with our core collapse simulations because of our mesh refinement, the neutrino radiation is not close to the free streaming limit until $r \gtrsim 100$ km, by that radius we have decreased our grid resolution, giving small effective CFL factors in these outer zones.

In Fig. 9, we show the radiation transport solution for the neutrino energy density. To achieve a constant value in the free streaming regime we scale the energy density by r^2. We normalize the data to range between 0 and 1. We show the solution after several light crossing times of the domain. The shadow cast by the absorbing torus is clearly seen and demon-

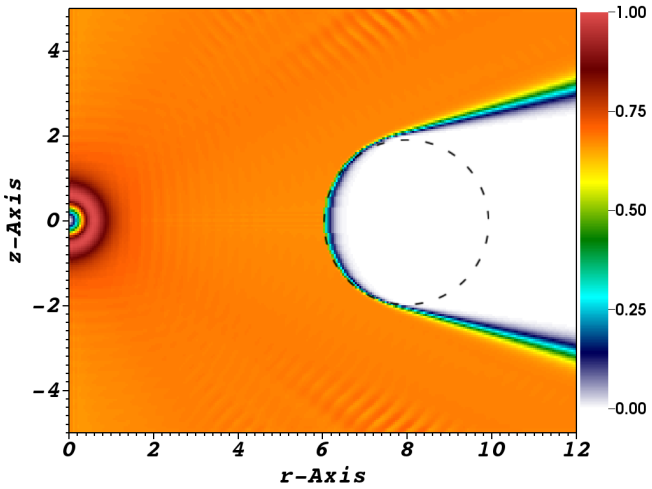

Figure 9. Neutrino energy density multiplied by r^2 in our M1 shadow test in 2D cylindrical coordinates. There is a spherical emission source located at the origin and a perfectly absorbing region (marked by the dashed circle) at $r = 8$ with a radius of 2. This test closely follows the setup of Just et al. (2015).

strates this ability of our code to maintain the neutrino momentum direction. There are slight artifacts seen as ripples at larger radii and along the coordinate axes nearer to the source that arising from the first-order explicit spatial flux integration.

REFERENCES

Audit, E., Charrier, P., Chièze, J., & Dubroca, B. 2002, arXiv:0206281
Baron, E., & Cooperstein, J. 1990, ApJ, 353, 597
Bethe, H. A., & Wilson, J. R. 1985, ApJ, 295, 14
Bruenn, S. W. 1985, ApJS, 58, 771
Bruenn, S. W., Lentz, E. J., Hix, W. R., Mezzacappa, A., Harris, J. A., Messer, O. E. B., Endeve, E., Blondin, J. M., Chertkow, M. A., Lingerfelt, E. J., Marronetti, P., & Yakunin, K. N. 2014, Accepted for publication in ApJ; arXiv:1409.5779
Bruenn, S. W., Mezzacappa, A., Hix, W. R., Lentz, E. J., Messer, O. E. B., Lingerfelt, E. J., Blondin, J. M., Endeve, E., Marronetti, P., & Yakunin, K. N. 2013, ApJL, 767, L6
Buras, R., Rampp, M., Janka, H.-T., & Kifonidis, K. 2006, A&A, 447, 1049
Burrows, A. 1988, ApJ, 334, 891
Burrows, A., Reddy, S., & Thompson, T. A. 2006, Nuclear Physics A, 777, 356
Burrows, A., & Sawyer, R. F. 1998, Phys. Rev. C, 58, 554
—. 1999, Phys. Rev. C, 59, 510
Colella, P., & Woodward, P. R. 1984, J. Comp. Phys., 54, 174
Colgate, S. A., & White, R. H. 1966, ApJ, 143, 626
Couch, S. M., & O'Connor, E. P. 2014, ApJ, 785, 123
Couch, S. M., & Ott, C. D. 2013, ApJL, 778, L7
—. 2015, ApJ, 799, 5
Dolence, J. C., Burrows, A., & Zhang, W. 2015, ApJ, 800, 10
Dubey, A., Antypas, K., Ganapathy, M. K., Reid, L. B., Riley, K., Sheeler, D., Siegel, A., & Weide, K. 2009, Parallel Comput., 35, 512
Ertl, T., Janka, H.-T., Woosley, S. E., Sukhbold, T., & Ugliano, M. 2015, ArXiv e-prints
Foglizzo, T., Scheck, L., & Janka, H.-T. 2006, ApJ, 652, 1436
Fryxell, B., Olson, K., Ricker, P., Timmes, F. X., Zingale, M., Lamb, D. Q., MacNeice, P., Rosner, R., Truran, J. W., & Tufo, H. 2000, ApJS, 131, 273
Handy, T., Plewa, T., & Odrzywołek, A. 2014, ApJ, 783, 125
Hanke, F. 2014, PhD thesis, Technische Universität München, München, Germany
Hanke, F., Marek, A., Müller, B., & Janka, H.-T. 2012, ApJ, 755, 138
Horowitz, C. J. 2002, Phys. Rev. D, 65, 043001
Just, O., Obergaulinger, M., & Janka, H.-T. 2015, MNRAS, 453, 3386
Keil, W. 1997, PhD thesis, Technische Universität München, Munich, Germany
Kuroda, T., Kotake, K., & Takiwaki, T. 2012, ApJ, 755, 11
Lattimer, J. M., & Swesty, F. D. 1991, Nucl. Phys. A, 535, 331
Lentz, E. J., Bruenn, S. W., Hix, W. R., Mezzacappa, A., Messer, O. E. B., Endeve, E., Blondin, J. M., Harris, J. A., Marronetti, P., & Yakunin, K. N. 2015, ApJL, 807, L31
Lentz, E. J., Mezzacappa, A., Messer, O. E. B., Liebendörfer, M., Hix, W. R., & Bruenn, S. W. 2012, ApJ, 747, 73
Liebendörfer, M., Mezzacappa, A., Thielemann, F.-K., Messer, O. E. B., Hix, W. R., & Bruenn, S. W. 2001, Phys. Rev. D, 63, 103004
Liebendörfer, M., Rampp, M., Janka, H.-T., & Mezzacappa, A. 2005, ApJ, 620, 840
Loken, C., Gruner, D., Groer, L., Peltier, R., Bunn, N., Craig, M., Henriques, T., Dempsey, J., Yu, C.-H., Chen, J., Dursi, L. J., Chong, J., Northrup, S., Pinto, J., Knecht, N., & Van Zon, R. 2010, Journal of Physics Conference Series, 256, 012026
Marek, A., Dimmelmeier, H., Janka, H.-T., Müller, E., & Buras, R. 2006, A&A, 445, 273
Marek, A., & Janka, H.-T. 2009, ApJ, 694, 664
May, M. M., & White, R. H. 1966, Phys. Rev., 141, 1232
Melson, T., Janka, H.-T., Bollig, R., Hanke, F., Marek, A., & Müller, B. 2015, ApJL, 808, L42
Misner, C. W., & Sharp, D. H. 1964, Phys. Rev., 136, 571
Müller, B., & Janka, H.-T. 2015, MNRAS, 448, 2141
Müller, B., Janka, H.-T., & Heger, A. 2012a, ApJ, 761, 72
Müller, B., Janka, H.-T., & Marek, A. 2012b, ApJ, 756, 84
Murphy, J. W., Dolence, J. C., & Burrows, A. 2013, ApJ, 771, 52
Nakamura, K., Takiwaki, T., Kuroda, T., & Kotake, K. 2015, PASJ
O'Connor, E. 2015, ApJS, 219, 24
O'Connor, E., & Ott, C. D. 2010, Class. Quantum Grav., 27, 114103
—. 2011, ApJ, 730, 70
—. 2013, ApJ, 762, 126
Ott, C. D., Abdikamalov, E., Mösta, P., Haas, R., Drasco, S., O'Connor, E. P., Reisswig, C., Meakin, C. A., & Schnetter, E. 2013, ApJ, 768, 115
Ott, C. D., Burrows, A., Dessart, L., & Livne, E. 2008, ApJ, 685, 1069
Pan, K.-C., Liebendörfer, M., Hempel, M., & Thielemann, F.-K. 2015, ArXiv e-prints
Rampp, M., & Janka, H.-T. 2002, A&A, 396, 361
Shen, H., Toki, H., Oyamatsu, K., & Sumiyoshi, K. 2011, ApJS, 197, 20
Shibata, M., Kiuchi, K., Sekiguchi, Y., & Suwa, Y. 2011, Progress of Theoretical Physics, 125, 1255
Sumiyoshi, K., Takiwaki, T., Matsufuru, H., & Yamada, S. 2015, ApJS, 216, 5
Suwa, Y., Kotake, K., Takiwaki, T., Whitehouse, S. C., Liebendörfer, M., & Sato, K. 2010, Pub. Astr. Soc. Jap., 62, L49
Suwa, Y., Yamada, S., Takiwaki, T., & Kotake, K. 2014, Submitted to the ApJarXiv:1406.6414
Takiwaki, T., Kotake, K., & Suwa, Y. 2012, ApJ, 749, 98
—. 2014, ApJ, 786, 83
Thompson, T. A., Burrows, A., & Pinto, P. A. 2003, ApJ, 592, 434
Wilson, J. R. 1971, ApJ, 163, 209
Woosley, S. E., & Heger, A. 2007, Phys. Rep., 442, 269
Woosley, S. E., Heger, A., & Weaver, T. A. 2002, Rev. Mod. Phys., 74, 1015
Woosley, S. E., & Weaver, T. A. 1995, ApJS, 101, 181